POLITECNICO DI TORINO

Master's Degree in Energy and Nuclear Engineering

Master's Degree Thesis

Monte Carlo simulations for shielding and activation of the 17 MeV MYRRHA injector beam line

Supervisors

Prof. Sandra DULLA

Dr. Yurdunaz ÇELIK

Dr. Alexey STANKOVSKIY

Candidate

Francesco PEPE

Ottobre 2023

Summary

The objective of the MYRRHA project is to couple a sub-critical reactor with a 600 MeV, 4 mA proton LINAC, as a very first prototype of Accelerator Driven System (ADS). In this configuration, the neutron population is sustained by the LINAC, which accelerates and focuses a proton beam to a spallation target inside the reactor.
The construction road map is divided into three phases. In the first phase, MINERVA, a research facility that will also function as the first section of the LINAC (up to 100 MeV), will be designed and constructed. In the second phase, the accelerator construction will be completed (600 MeV). In the third phase, the reactor will be built.
According to current estimates, the construction will be completed in 2036, with MINERVA already available in 2026. For the complete design of MINERVA, many aspects still need to be considered and, most importantly, its safe operation must be fully demonstrated. This thesis focuses on the shielding and activation of the first component of MINERVA, the injector, in which protons are accelerated from 30 keV (at which they are generated in the ion source) to 17 MeV, and its beam dump, which will absorb a maximum of 68 kW of proton beam energy (17 MeV, 4 mA). This last component will be used during the injector commissioning and maintenance tests.
The objective of this thesis is to demonstrate that the shielding provisions suggested so far at SCK CEN, and the ones that are suggested in this work, are enough to guarantee that the safety standards for people and environment are respected.
Two types of radiation sources are responsible for radiation along the beam line, and around the beam dump.
The large amount of prompt doses and radioactivity in the beam dump and in its shield are produced due to interactions of the primary protons with the beam dump materials. As far as the beam line is concerned, continuous proton beam losses (1 W/m) along the beam line are assumed. Radiation will be created due to the interaction of the lost protons with the beam line components and the surrounding materials. The shielding design of the injector and of the beam dump is done by means of the Monte Carlo transport code MCNP6.2, developed at the

Los Alamos National Laboratory. Activation calculations are performed with the SCK CEN depletion code ALEPH2. In order to speed up the calculations and to obtain better statistics, a massive use of variance reduction techniques is made. In particular, mesh-based weight windows and DXTRAN spheres are studied and applied. The results obtained with these tools show that it is possible to satisfy the safety requirements concerning the dose rate limits imposed by the Belgian legislation and by SCK CEN, by implementing simple shielding designs, based on concrete and other shielding materials. In particular, dose rates inside and outside the injector tunnel are calculated. Thanks to these results, it is possible to demonstrate that the dose rate outside the injector tunnel is below the dose rate limit for workers. Moreover, the dose absorbed by some internal devices, such as the lighting fixtures inside the tunnel, are computed, in order to suggest a maintenance and replacement strategy. An entrance is foreseen to access the injector tunnel, in case of maintenance. During normal operation, a shielded door must be used in order to shield workers outside of the tunnel. In this work, a simple three-layers layout is proposed for the shielded door, featuring the use of lead and borated polyethylene, which have been proven to be effective in photon and neutron shielding, respectively. For the beam dump, a shielding design was already proposed at SCK CEN. Its effectiveness is demonstrated by this work, and the activation of the concrete is studied.

Acknowledgements

A Viggiano, Torino, Boeretang

Table of Contents

List of Tables

List of Figures

Acronyms

SCK CEN (Belgian Nuclear Research Center)
MYRRHA (Multi-purpose hYbrid Research Reactor for High-tech Applications)
ADS (Accelerator Driven System)
MCNP6.2 (Monte Carlo N-particle)
VOV (Variance of Variance)
FOM (Figure of Merit)
LINAC (Linear Accelerator)
LEBT (Low Energy Beam Transport)
RFQ (Radio Frecuency Quadrupole)
CH (Cross-bar H-type cavities)

Chapter 1

Introduction

1.1 The MYRRHA project

MYRRHA (Multi-purpose hYbrid Research Reactor for High-tech Applications) will be the first large scale ADS (Accelerator Driven System) in the world [1]. This system is characterized by the coupling of a sub-critical nuclear reactor with a high power linear accelerator (Figure 1.1).
This ambitious project is being developed at the Belgian Nuclear Research center (SCK CEN), in Mol. As the name suggests, MYRRHA developers want to pursue many objectives. First of all, it will demonstrate the feasibility of the ADS concept at pre-industrial level. Other purposes are the research and development on transmutation and waste minimization, on linear accelerator, on irradiated materials and the production of medical isotopes.
MYRRHA will be a lead-bismuth cooled fast reactor and two configurations will be possible: critical or sub-critical. When it is in sub-critical configuration, the neutrons population is sustained by the accelerator. This component accelerates and focuses a proton beam to a spallation target inside the reactor. Protons will undergo spallation reactions there, from which neutrons will be produced [2].
The MYRRHA accelerator will be 400 m long and will accelerate protons up to 600 MeV. The reference technology is the linac, which was chosen due to its very high stability, especially when compared to other similar technologies, such as the cyclotron. Moreover, its design guarantees high degree of reliability. This is achieved thanks to redundancy in some key components, such as the two redundant 17 MeV injectors.
According to the construction road map, the whole facility will be built in three phases[1]. The first section of the linac, MINERVA, will accelerate protons up to 100 MeV. The construction of MINERVA will end in 2026. In the second phase, the linac construction (up to 600 MeV) will be completed. In the third phase, the

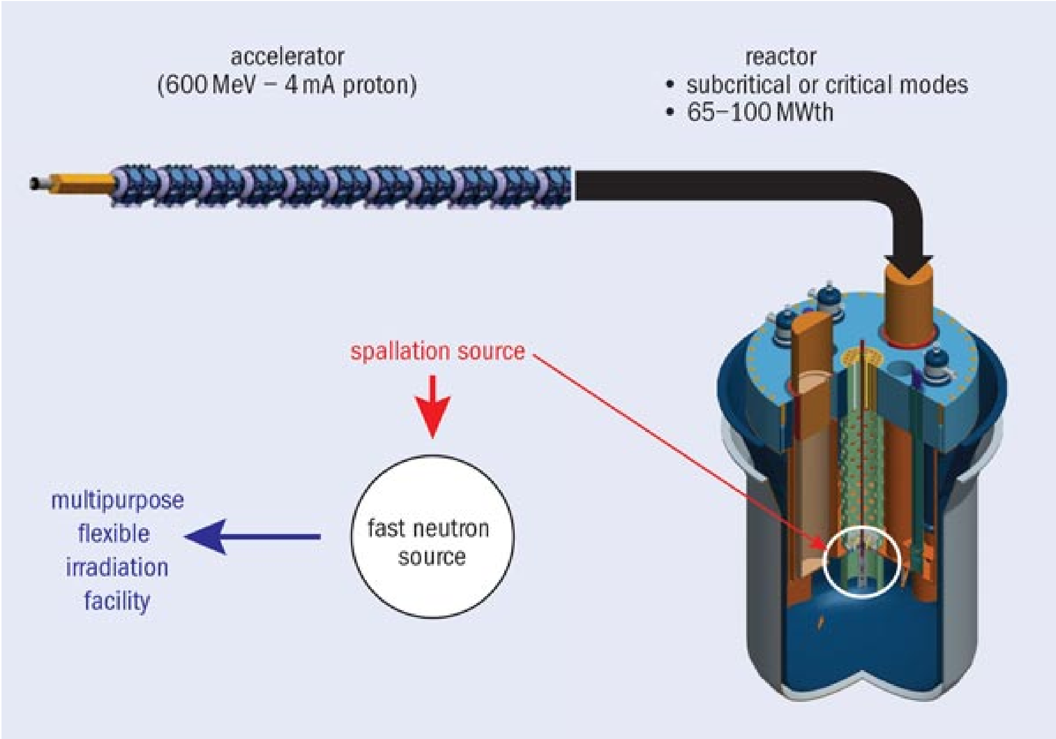

Figure 1.1: MYRRHA: accelerator and reactor coupling [1].

reactor will be built. This last phase will end in 2036.
For the complete design of MINERVA, many aspects still need to be considered and, most importantly, its safe operation must be demonstrated. This thesis focuses on the shielding and activation of the first component of MINERVA, the injector, in which protons are accelerated to 17 MeV. The objective is to demonstrate that the shielding provisions suggested so far at SCK CEN, and the ones that will be suggested in this document are enough to guarantee that the safety standards for people and environment are respected.

1.2 Shielding and activation

Shielding and activation of materials are some of the major topics in the design of nuclear or nuclear-related facilities.
Shielding calculations are required to assess the performance of shielding configurations and materials, which are used to reduce the radiation arriving to a certain target. In particular, shields can be used to protect workers and the public, but also to reduce the dose absorbed by devices which may be irreversibly damaged by radiation.

When placed in a neutron radiation field, a certain material can experience activation. This happens due to neutron-induced reactions, leading to the formation of radioactive nuclei. The activities of these products may be very different and their half-lives may range from fractions of second to millions of years. The radiation that they emit, that can be alpha, beta or gamma, must be determined so that protection measures can be adopted. For this reason, it is important to understand what are the activation products, and what is the induced residual radiation field. These phenomena are particularly important and evident in particle accelerators, especially due to the high energies that the particles can reach. The safe operation, the operational life and the overall performance of this type of device is strongly influenced by the capacity of shielding the workers and the external environment. Moreover, the degree of activation of components at the end of their operational life can determine the classification of the materials as waste.

1.3 Objectives

The aim of the MYRRHA project is to couple a sub-critical reactor with a 600 MeV, 4 mA proton LINAC. Protons along the beam line are accelerated and focused by several accelerator components. In particular, three main energy sections (17 MeV, 100 MeV and 600 MeV) can be identified in the beam line.
The focus of this thesis is on the first section of the MYRRHA accelerator: the normal conducting injector, which accelerates the beam from 30 keV to 17 MeV. In this framework, prompt and residual dose rates, and radioactivity of the beamline and beam dump components should be determined, in order to provide safe and efficient operation, including maintenance activities.
The performance of the shielding components, the activation of the materials, and the compliance of the legislative and SCK CEN dose limits are assessed with simulations, performed via the Monte Carlo code MCNP6.2 [3] and the activation calculation code ALEPH-2.8 [4].
In order to pursue this objective, at first, a theoretical study of the Monte Carlo method and of the main variance reduction techniques will be conducted. After that, a series of practical tasks related to the injector will be performed.
Most of these tasks are dose rate calculations, which are performed: to verify the respect of a certain limit for workers exposure; to compute the absorbed dose of some specific devices that are placed inside the injector tunnel, in order to propose a maintenance and replacement strategy; and to propose a strategy to reduce the dose in specific areas (ex. the injector entrance). Activation calculations are performed for the beam dump and its concrete shield.
In summary, the tasks to be performed are the following:

- Dose rate attenuation in the concrete shield of the injector tunnel;

- Absorbed dose for the lighting fixtures;
- Dose rate assessment at the injector entrance;
- Shielding door design for the injector entrance;
- Dose rate attenuation in the concrete shield of the beam dump;
- Activation of the beam dump.

The results of this thesis will provide an outlook on the state of the shielding and activation of the MYRRHA injector, and may be taken as a starting point for a future more detailed design of this fundamental component.

1.4 Structure of the thesis

After the short introduction contained in this chapter, the main steps of this work are presented, from the identification of the context to the discussion of the numerical results. Excluding the introductive chapter, this thesis is divided in the following chapters:

- **General context and problem description**: the objectives, the conceptual design and the state of the work of the MYRRHA project are summarised. After that, a focus is presented on the geometry of the components of interest for this work: the beam line and the beam dump. A description of shielding requirements at SCK CEN closes this chapter.
- **Calculation tools and techniques**: here, a presentation of the codes used in this work (MCNP and ALEPH) is done. An insight on the variance reduction techniques, which have been extensively used in all the simulations, is given.
- **Simulation setup**: here, the main choices about the simulation setup are presented and discussed, with a particular focus on the geometry of the problem, the source and the tally definition.
- **Simulations and results**: the simulations and the results are presented in this chapter.
- **Conclusions and future perspectives**: the main findings of the work are summarised and commented again, here. Some suggestions on next steps for the continuation of this work are given.

Chapter 2

Problem description

2.1 Injector geometry

As schematized in Figure 2.1, the 100 MeV MINERVA beam line is composed of two sections: the injector and the superconducting tunnel. The injector beam line accelerates protons from 30 keV, at which they are generated, to 17 MeV [1]. The length of this section is in the order of tens of meters (about 40 m) and is composed of a proton source, the Low-Energy Beam Transport line (LEBT), the Radio-Frequency Quadrupole (RFQ), and a series of CH cavities. At the end of the injector section, a beam dump (BD) is located [5].
The superconducting tunnel will bring protons' energy up to 100 MeV, but it is not the object of this work.

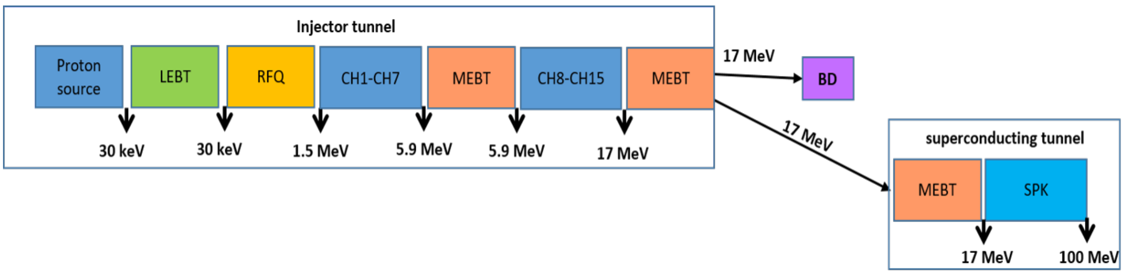

Figure 2.1: MINERVA beam line [5].

2.1.1 Beam line

MINERVA ion source can produce a current up to 16 mA of protons at 30 keV. It is based on the Electron Cyclotron Resonance technology, which exploits ionization through radio frequency radiation in a magnetically confined plasma to separate ions and electrons [6] .
The LEBT connects the proton source to the first section of the accelerator, the RFQ. The function of the LEBT is to transport and focus the protons in the right direction. Protons are transported thanks to a magnetic field along its axis, which is created by two solenoids, at the beginning and at the end of this component. More windings are used to focus the beam and a beam chopper at the end of the LEBT to regulate the beam intensity. [6]
The first component where protons experience a real acceleration is the RFQ, where their energy increases from 30 keV to 1.5 MeV. It is composed of a copper tube surrounded by an aluminum square section cylinder [7]. In Figure 2.2, the cross section of the CAD model of the RFQ is shown.

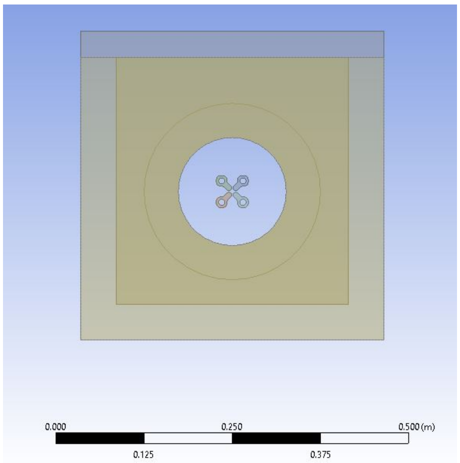

Figure 2.2: RFQ cross section.

15 Cross-bar H-type (CH) cavities are used in the rest of the injector to reach about 17 MeV. They are all made of two coaxial stainless steel cylinders with perpendicular inner rods, but they have different lengths. In particular, the length progressively increases from the first to the last CH cavity [8]. The CAD model of the first CH cavity is shown in Figure 2.3.
Knowing how the different components are made and what are their relative positions is important to understand how the proton beam will be, in terms of energy and orientation. For instance, information about the active lengths and the positions of the RFQ and of the CH cavities is used to model proton source in the

MCNP input file.

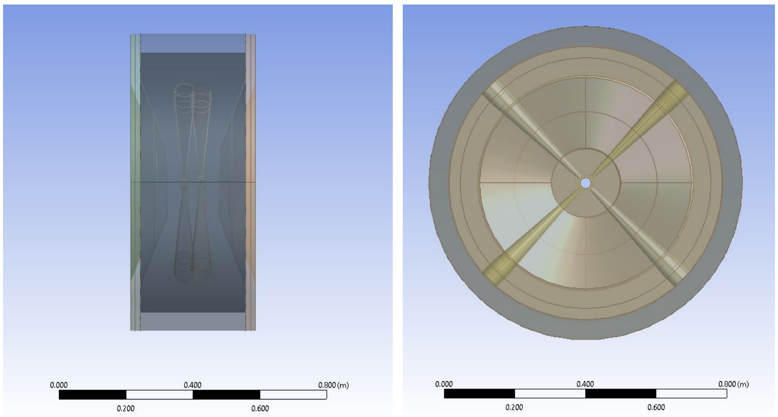

Figure 2.3: CAD model of the first CH cavity. Axial view on the left, cross section on the right.

2.1.2 Beam dump

The conceptual model of the beam dump assembling is shown in Figure 2.4. The proton beam hits the flat surface of a series of 'mushrooms', inserted in and tightened to a CuCrZr bar. Cooling is provided by water flowing in cooling channels. Moreover, to increase the area on which the beam is deposited the beam dump shall be at an inclination of 6°.

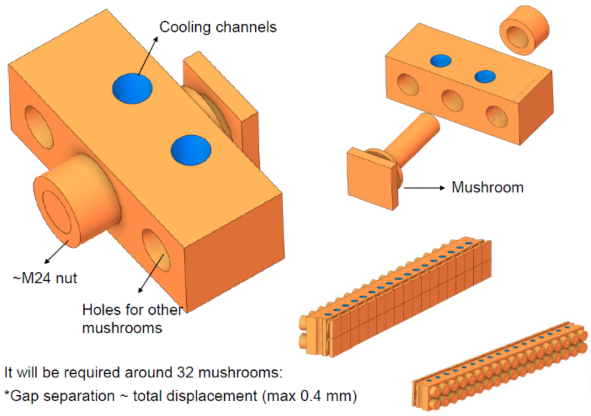

Figure 2.4: conceptual model of the injector beam dump. Protons will hit the flat tiles of the 'mushrooms'.

2.2 Shielding requirements and clearance

The Belgian legislation sets a limit to the effective dose of 20 mSv/y for exposed workers, and of 1 mSv/y for non-exposed workers and general population [9]. In accordance with the ALARA principle, SCK CEN adopts a dose constraint, imposing a limit of 10 mSv/y to the exposed workers. Considering 2000 operation hours per year, this limit can be converted to 5 μSv/h.
At SCK CEN, the typical classification of supervised and controlled areas is considered. The controlled area is an area for which specific protection and safety provisions are required, in order to control the normal exposure and to prevent the spread of contamination. The supervised area is an area for which occupational exposure conditions are kept under review, even though no specific protection measures or safety provisions are normally needed [10].
The SCK CEN limit for the controlled area is set to 5 μSv/h, while for the supervised area it is 1.5 μSv/h. As design criterion for MINERVA, a safety factor of 2 has been adopted. This criterion is needed in order to take into account systematic uncertainties related to computer code simulations, differences in the material composition, manufacturing tolerances of components, etc. As a result of that, the limits generally considered for the MINERVA controlled and supervised areas are 2.5 μSv/h and 0.75 μSv/h.
As far as activation is concerned, the exemption limit of 1 Bq/g is assumed. Clearance is defined as the removal of the radioactive materials or radioactive objects within the authorized practices from any further regulatory control by the regulatory body [11].

Chapter 3

Calculation tools and techniques

3.1 MCNP6.2

The shielding simulations for the 17 MeV MYHRRA injector beam line are performed with the radiation transport code MCNP6.2 (Monte Carlo N-particle), which is developed and maintained by the Los Alamos National Laboratory [3] and is considered the reference particle transport code at SCK CEN. MCNP6.2 is used to analyze the behavior of particles in complex systems. Particle transport and interactions are simulated by means of the Monte Carlo method. It is widely used in a variety of fields, such as nuclear physics, radiation protection and neutronic design of reactors and particle accelerators.
For neutrons, the reference basic nuclear data library is based on JEFF-3.3 [12], which adopts TENDL-2017 as proton sub-library [13].

3.2 ALEPH2

The depletion code ALEPH2 is used for activation calculations [4]. This code is developed at SCK CEN. The objective of the developers is to fill the gap between steady state Monte Carlo transport and time dependent depletion calculation. ALEPH2 uses MCNP to perform steady state transport calculation, whose solution are fluxes and spectra. These are used to compute reaction rates, that are used in subsequent depletion and activation calculations. A very simple scheme is in Figure 3.1.
One of the main advantages of ALEPH2 is its simplicity. The input file is basically an extension of the MCNP input, with a limited number of additional cards. In

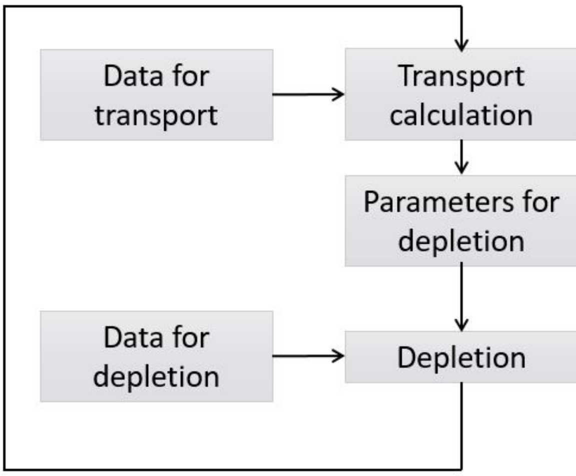

Figure 3.1: simple ALEPH scheme.

particular, the number and the volumes of the materials that the user wants to study, and the time steps at which the solution is computed must be requested must be specified. In the input file, it is possible to request a variety of parameters to be given with the solution. Some example are total and specific activities, elemental and isotopic concentration, heating due to radiation and delayed radiation spectra for alpha, beta and gamma decay of the radioisotopes.

3.3 Quality of the results and statistical tests

The results of a Monte Carlo simulation can be considered acceptable when they are accurate and precise. Accuracy is a measure of the difference between the sample average $\bar{x}$ and the value of the true physical quantity, whose estimation is the objective of the simulation. This distance is also known as systematic error, and it is usually not known a priori. Accuracy may depend on a series of factors such as errors in the code, uncertainties on the input data, wrong modelling of the physics of the problem and user's errors.
On the other hand, precision is related to the statistical fluctuation of the random walk scores x_i sampled in the phase space of the computational model. It can be dramatically affected by the type of simulation, by the number of histories and by the implementation of variance reduction techniques. In order to assess the precision of the results, 10 statistical tests are automatically performed by MCNP6 [3]. These tests are satisfied if:

1. Mean value is random at least for the last half of the problem. This means that

the mean behavior is non-monotonic as a function of the number of histories N;

2. The relative error R is less than 10 %(at least for non-point or ring detectors);
3. The relative error R decreases monotonically for the last half of the problem;
4. The relative error R decreases as $1/\sqrt{N}$ for the last half of the problem;
5. The variance of variance VOV is less than 10
6. The variance of variance VOV decreases monotonically for the last half of the problem;
7. The variance of variance VOV decreases as $1/\sqrt{N}$ for the last half of the problem;
8. The figure of merit FOM remains statistically constant for the last half of the problem;
9. The figure of merit FOM exhibits a non-monotonic behavior in the last half of the problem;
10. The slope of the pdf f(x) is greater than 3.

3.4 Variance reduction techniques

The objective of a Monte Carlo simulation is to obtain an acceptable tally estimate within a reasonable computing time. As discussed in the previous section, the quality of the tally estimate is strictly linked to the estimated relative error, defined as:

$$R = \sigma_{\bar{x}}/\bar{x} \tag{3.1}$$

where $\sigma_{\bar{x}}$ is the standard deviation of the mean. $\bar{x}$ is the mean.
In general, R is proportional to $\sigma_{\bar{x}}/\sqrt{N}$, with N the number of histories.
The relative error is very useful to understand what is the range of values in which the true result may fall. In fact, as a consequence of the Central Limit Theorem [14], when N approaches to infinite, the true result lies in the interval $\bar{x}(1 \pm R)$ with a 68% probability, and in the interval $\bar{x}(1 \pm 2R)$ with a 95% probability.
Since the computing time T increases with the number of histories N, then $T \sim N$ and

$$R \sim \sigma_{\bar{x}}/\sqrt{T}. \tag{3.2}$$

Thus, two paths can be followed in order to decrease the error: reducing σ or increasing T [15]. In most of the cases, results are needed within a given period of time, and increasing the computational time does not seem the most efficient option. For this reason, techniques have been developed with the objective of reducing the variance.

3.4.1 Analog and non-analog Monte Carlo

An analog Monte Carlo simulation uses the natural probability that a certain event (fission, capture, scattering, etc.) occurs. Each particle track is followed, and the next event is sampled on the basis of the natural probabilities of all the possible next events. Each history contributes to the tally estimate with a score, but if a particle does not reach the tally region, then its score will be zero. Analog Monte Carlo fails when the number of particles effectively contributing to the tally estimate is very small (less than 10^{-6}).
A non-analog simulation preferentially follows "interesting particles", i.e. those particles that contribute the most to the final result. In other words, it allows to artificially increase the number of particles reaching the tally region, without changing the tally value. In order not to bias the result, a statistical weight is assigned to each particle and it is decreased as the particle is forced towards the tally region. Thus, if the likelihood that a particle will execute a certain random walk is increased of a factor q, the associated weight is reduced of $1/q$. This permits to preserve the average score, and the non-analog tally estimate will be the same as the analog one.

3.4.2 Techniques

There are four classes of variance reduction techniques: truncation, population control, modified sampling, and partially-deterministic methods [3].
Truncation methods
Truncation methods work by truncating parts of the phase-space. For example, in the rare case in which the user knows a priori that a part of the geometry is not important for the estimate, this can be disregarded. Other types of truncation methods are energy and time cutoff.
Population control
To control the number of sampled tracks, population control methods can be used in different regions of the sample space. These methods are based on the principle that many samples of small weight are tracked in important regions, while few large weight samples are tracked in less important regions. In order to do so, splitting and Russian roulette are usually implemented.
Splitting consists in dividing the weight of a particle w_0 among a certain number k

of daughters and following them independently. In most of the cases, the weight is equally divided among the k identical daughter particles, which in turn will have weight w_0/k, but also other cases in which the daughter particles are not exactly identical may exist.
When Russian roulette is played, instead, a certain particle of weight w_0 is killed with a certain probability $(1 - w_0/w_1)$. If the particle survives, then its weight is increased to $w_1 > w_0$.
Even though they can be used separately, splitting and Russian roulette are usually implemented together. The easiest way to understand their behaviour is by considering the so-called geometry splitting/roulette, which is based on the difference in the importance of different cells. In fact, the user can specify a certain importance I for each cell of the geometrical domain. When a particle in a cell of importance I enters a cell of importance $I' > I$, the particle is split in a number of daughter particles of lower weight. If the contrary happens (i.e. $I' < I$), Russian roulette is played. A simple example is shown in Figure 3.2, in which $I_2 > I_1$.

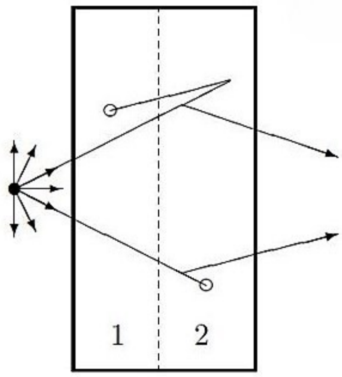

Figure 3.2: splitting and Russian roulette [3].

Other population control methods are energy splitting/roulette, time splitting/roulette.
Modified sampling
In order to better sample important regions, the statistical sampling can be altered with modified sampling methods. Instead of using the physical probabilities, arbitrary distributions that send particles in certain preferential directions can be used. In Figure 3.3, an example of source biasing is depicted: an isotropic source (a) is modified in order to consider only particles emitted in the direction of the detector (b).
Partially-deterministic methods
Finally, partial deterministic methods can be implemented. They change the normal random walk process by using deterministic-like techniques.

In this work, the main techniques that have been implemented are Weight Windows and DXTRAN. Thus, their description will be assessed with major details in the following sections.

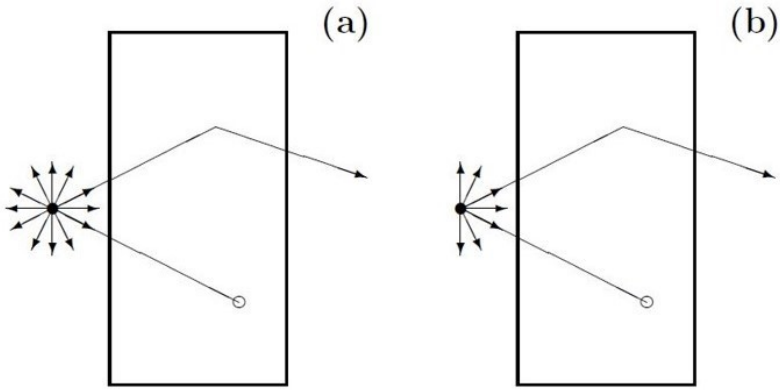

Figure 3.3: analog source (on the left) and biased source (on the right) [3].

3.4.3 Weight windows

Splitting and Russian roulette are the processes at the basis of the weight windows technique. For each cell, a lower (W_L) and an upper (W_U) weight bounds are defined. In particular, the user can specify the lower bound, and the upper one will be a predefined multiple of it. Lower and upper limits define a window of possible weights [16]. Particles entering a cell with a weight that is above the upper bound are split, so that all the daughter particles have weights within the window. On the contrary, Russian roulette is applied to particles whose weight is below the lower bound. If the particle survives, its weight is increased to a value (W_s) within the window. The process is schematized in Figure 3.4.
In general, lower weight bounds can be defined by the user on the basis of experience and intuition, but this can be very difficult to perform. In this work, the WWG (Weight Window Generation) card has been used to generate mesh based weight windows. The resulting lower bounds are themselves estimates, and thus they are affected by an error. The user must be able to assess how big is that error and to discern between acceptable and unacceptable values.

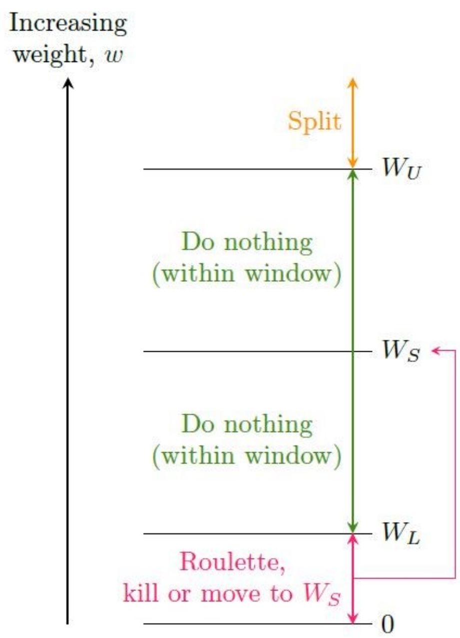

Figure 3.4: weight windows basic process [3].

3.4.4 DXTRAN

DXTRAN is an angle-biasing technique that can be used to improve the statistics in cells that would be otherwise inadequately sampled [17]. Thus, this technique is particularly useful to sample small regions for which particles have a low probability of scattering towards.
Practically, the user can define a DXTRAN sphere that completely encloses the region that he wants to sample. Upon each collision outside the sphere or at the source, a DXTRAN and a non-DXTRAN particles are created. The DXTRAN particle is deterministically scattered, without any other collision, to the surface of the sphere, while the non-DXTRAN particle is sampled in the normal way, but it is killed in case it tries to enter the sphere. A simple scheme of this process is shown in Figure 3.5. The weight of the non-DXTRAN particle is not reduced so, in order not to bias the result, the extra weight that the DXTRAN particles carry on the sphere must be balanced by the weight of the non-DXTRAN particles killed on the sphere [17].
The choice of maintaining the same weight for the non-DXTRAN particle may be difficult to understand, but it can be better explained according to two viewpoints of the same process [3].
First of all, the DXTRAN can be interpreted as a splitting process, in which two

particles are created: the non-DXTRAN particle with weight w_1 and the DXTRAN particle with weight w_2. Upon collision, the first particle may or may not enter the DXTRAN sphere on its next collision with probabilities p_1 and p_2, respectively. One may think of assigning weight $w_1 = p_1 \cdot w_0$ to the non-DXTRAN particle, with w_0 weight of the particle before the collision. In reality, this is not done because the probability p_1 is not known a priori, and the weight assigned to the particle is w_0. The reason is that a Russian roulette game is played, in which the non-DXTRAN particle is killed with a probability p_2 (i.e. if it tries to enter the DXTRAN sphere) and, if it survives (with probability $p_1 = w_1/w_0$), its weight is increased to w_0. This way, the expected weight not entering the DXTRAN sphere is as desired: $w_0 \cdot p_1 + 0 \cdot p_2 = w_1$.
Alternatively, DXTRAN can be seen as a process in which weight is both created and destroyed on the surface of the DXTRAN sphere. The weight that goes to the sphere is estimated and created on the surface of the sphere as a DXTRAN particle. Thus, the weight crossing the sphere is all taken into account by the DXTRAN particle and if the non-DXTRAN particle tries to enter the sphere, it must be killed in order not to have an excess of weight.

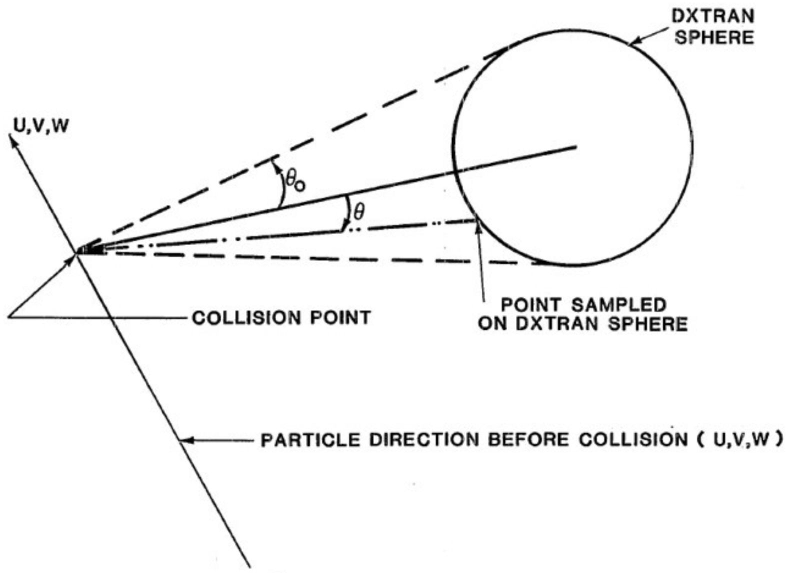

Figure 3.5: DXTRAN basic process [3].

In conclusions, weight windows and DXTRAN spheres can both be used to improve the statistics in a certain region of interest, where the tally is placed. They can be used effectively together or not, depending on the situation. In particular, DXTRAN spheres can be used in free streaming problems, for example in corridors or entrances. In case of dose attenuation calculations in thick shields, the use of weight windows alone is generally preferred.

Chapter 4

Simulation setup

While compiling the input file of a simulation, it is important to have clear in mind what are the quantities that we want to estimate, and what is the information that we need, in order to setup the calculation. In this chapter, a summary of the main choices in the simulation setup is presented.
At first, the geometry definition and the main simplifications that have been considered are described. After that, the the source and its definition in MCNP6.2 is discussed. In the last section of the chapter, the main tallies that have been used are listed.

4.1 Injector and beam dump geometry

As discussed in the second chapter, the actual geometries of both the beam line and the beam dump are not trivial, since they are made up of many different components.
Nevertheless, modeling all the components with a high degree of detail would be very time consuming and would increase a lot the level of complexity of the problem, both from a modelling and calculation efficiency points of view. In fact, having a larger number of cells usually reduces the efficiency of the calculation and may counterbalance the effect of variance reduction techniques. For the purpose of this thesis work, the simplified model shown in Figure 4.1 has been used.
Vacuum is assumed inside the beam tube, and there is air in the tunnel outside of it. The air tunnel is surrounded by a concrete wall and soil. The choice of not considering all the beam components is considered to be conservative in the shielding calculation that are performed in this work. In fact, without them, less neutrons and photons will be stopped before reaching the injector walls. This is true for the case in analysis, in which all protons are lost with a preferential direction (forward), even if with a certain grazing angle. In case of streaming in

other directions, particles may be back-scattered by the surrounding components and the choice that has been made would not be conservative. Fortunately, this is not the case for the problem in analysis.
Also the beam dump can be definitely simplified. Instead of considering the subdivision of its flat surface in 'mushrooms', a single CuCrZr can be used, and the cooling channels can be neglected.
In Figure 4.2-top, the 3D CAD model of the beam dump is shown. In Figure 4.2-bottom, the MCNP model of the void and the vacuum pipe that connect the injector tunnel to the beam dump, and the beam dump itself are represented.

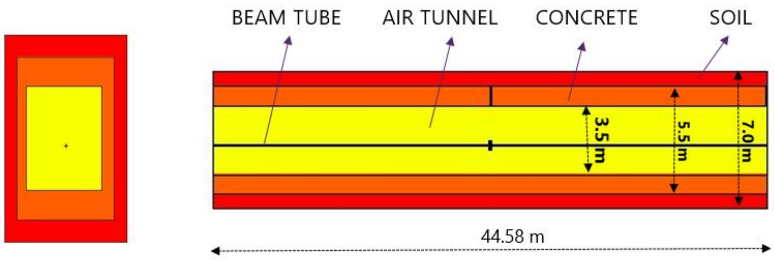

Figure 4.1: simplified model of the beam line.

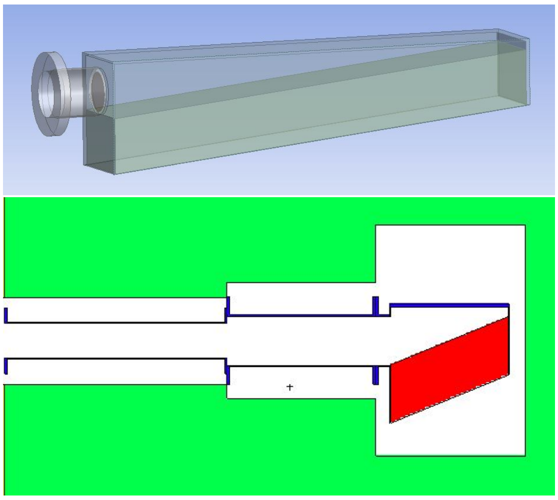

Figure 4.2: simplified CAD model of the injector beam dump (top). simplified model of the injector beam dump (in red, CuCrZr), and pipes (in blue, steel) (bottom). Proton beam is impinjing from the left.

4.2 Source definition

For most of the shielding calculations that will be described in this thesis, the focus is on the injector beam line and tunnel. As discussed in the previous sections, dose rates are requested for different areas and elements of the injector tunnel. In all these cases, the source can be considered the same, as the radioactivity in the tunnel is mostly due to the secondary neutrons and photons created by the interaction of the protons lost in the beam line and the surrounding components (beam tube, mainly).
As far as the beam dump is considered, modeling the whole beam line would be counterproductive. Moreover, the cause of the activation of the beam dump components, and the dose rates in the concrete shield are not due to the proton losses, but to the direct impact of the proton beam on the beam dump.
In this chapter, the particle source definitions used in MCNP6.2 for the beam line and beam dump models are described and discussed.

4.2.1 Beam line

Beam losses are the main cause of radiation in the injector tunnel, because of the interaction of lost protons with the beam line components and the surrounding materials. For all existing LINACs, the value of the beam losses considered in the design is in the order of 1 W/m, in normal operating conditions [18] [19] [20]. The same value for the beam losses and a grazing angle of 15 mrad [21] have been considered in this work.
In the injector, protons are accelerated from 30 keV to 17 MeV. Thus, particles will be lost at different energies in different positions. For the purpose of this work, two configurations have been analyzed:

1. a simplified but conservative source definition, in which all protons are lost at the same energy of 17 MeV;

2. a more realistic case, in which protons are lost at different energies depending on their position.

In both cases the proton current can be calculated dividing 1 W/m by the energy of the protons in a certain trait. If the proton current is then divided by the charge of the proton, the number of protons lost per second in a meter length is obtained. With this process, it can be derived that 3.67E+11 p/s/m are lost along the beam line in the first configuration.
In Figure 4.3 (top), the energy increment and the beam losses along the beam line are shown for the second configuration. The energy increments are based on the expected increase of the protons energy in the different components of the

beam line, as reported in the appendix B. The beam losses are calculated with the procedure that has been previously described.
In order to simulate the proton beam losses in MCNP6.2, a point-wise distribution of the beam losses (p/s/m) as a function of the position (cm) has been specified in the input file. MCNP6.2 interpolates these values linearly, thus the integral of the distribution can be calculated with the trapezoidal rule. This way, the total losses are found. For the distribution described in Figure 4.3 (bottom), the integral value is 5.07E13 p/s. This number is important because it also represents the normalization factor for all the results in MCNP6.2.

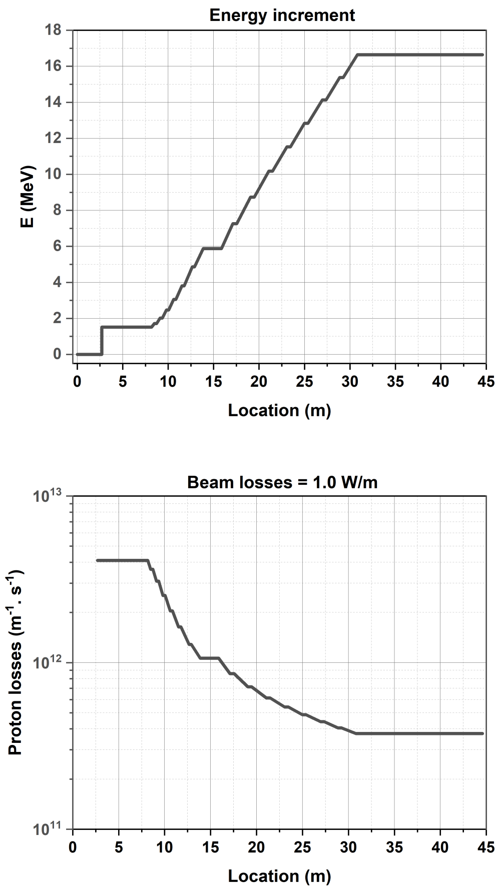

Figure 4.3: Energy increment and beam losses along the beam line.

4.2.2 Beam dump

The beam dump will not be absorbing a continuous wave beam. Only a few pulses of the proton beam shall be sent to the injector beam dump, the rest of the beam is chopped by the chopper. An example of the beam pulses that might be sent to the injector beam dump is shown in Figure 4.4.

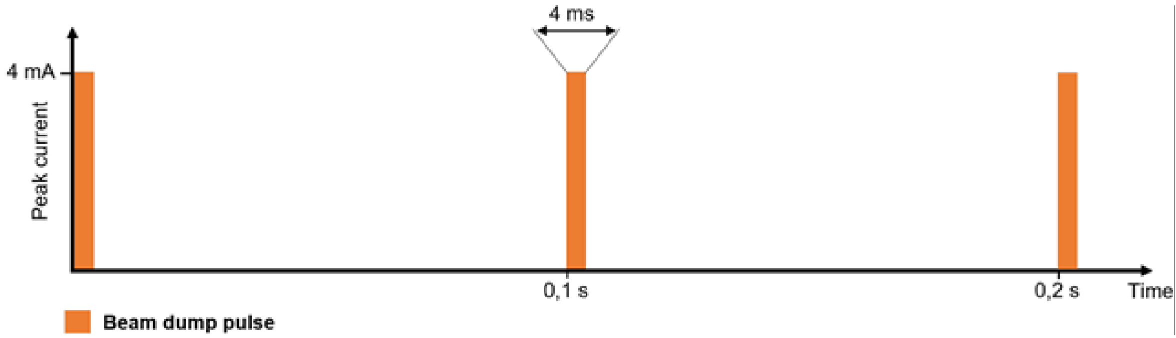

Figure 4.4: Example of beam pulses that might be sent to the beam dump.

The nominal beam energy and proton current are 17 MeV and 4 mA. With a full duty cycle this results in an average power dissipation of 68 kW. Nevertheless, at a reduced duty cycle of 5 %, this results in 3.5 kW on average.
To include a certain safety margin, an average power dissipation of 5 kW can be assumed (i.e. 17 MeV and 0.3 mA).
The proton source should be a uniform cylindrical beam, with an external diameter of 72 mm, and directed towards the center of the beam dump. In MCNP6.2, this is modelled with a disk source of 36 mm radius and direction of emission along the positive x-axis (towards the beam dump).

4.3 Tally and dose rate calculations

In MCNP6.2, a vast choice of tallies is possible. The four types of tally that have been used in this work are the $f2$, $f4$, $f6$ and $fmesh4$, which are quickly described in the following lines.
All the results are actually normalized to the source particles, which in the simulations of this work are always protons. Thus, it is important to multiply the MCNP output by the number of protons emitted by the source per second.
$f2$, $f4$ are the average surface flux and average cell flux tallies, respectively. They both provide rates in [#/cm^2], and are defined as follows:

$$F2 = \frac{1}{A}\int_A dA \int_E dE \int_{4\pi} d\Omega \Phi(r_s, E, \Omega) \tag{4.1}$$

$$F4 = \frac{1}{V}\int_V dV \int_E dE \int_{4\pi} d\Omega \Phi(r_s, E, \Omega) \tag{4.2}$$

where S is the surface through which the flux is calculated, and V is the cell volume.
$fmesh$ tallies the same quantity, but averaged on a mesh cell. It can be useful to study regions in which information about smaller portions of a geometry cell is needed, and to produce dose rate maps.
The $f6$ tally provides the energy deposition in a certain cell for a specific type of particle, in [MeV/g].
If the effective dose rates need to be calculated, the result in μSv/h, can be obtained by using the particle flux to ambient dose equivalent conversion factors (pSv·cm^2), which are plotted in Figure 4.5. Both the values for neutrons and photons have been taken from the ICRP report 74 [22]. Dose conversion factors are energy dependent functions $DCF(E)$. The $DCF(E)$ is added to the equation Equation 4.2 and integrated over energy.

To convert the results to μSv/h, the multiplication factor MF in Equation 4.3 is used, where [protons/s] is the number of protons per second emitted by the source and depends on the source definition.

$$MF = 10^{12}(Sv.cm^2) \cdot 10^6(\mu Sv/h) \cdot 3600(s/h) \cdot [protons/s] \tag{4.3}$$

The absorbed dose rate in Gy/y can be obtained from the $f6$ tally, using, also in this case, the normalization factor given by the proton source, and by converting MeV to J.

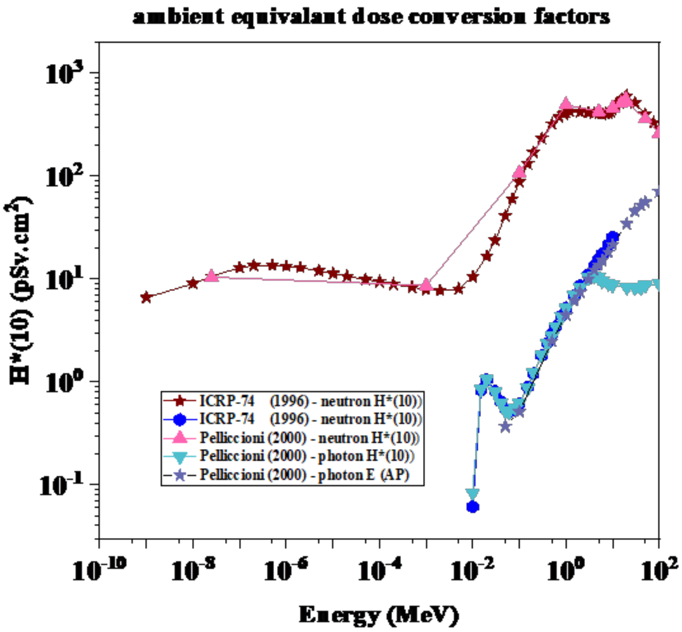

Figure 4.5: particle flux to ambient dose equivalent conversion factors.

Chapter 5

Simulations and results

5.1 Dose rate attenuation in the concrete shield

The aim of this simulation is to compute the dose rates in the concrete layer (1 m thickness), and to verify that this is enough to satisfy the dose limit set for the MINERVA controlled zone (2.5 μSv/h). This verification has been implemented in two simulations, with different source definitions (all protons generated at the same energy or with increasing energy), so that a comparison can be made between the two cases.
In both simulations, 10 detectors of 1 cm thickness each are placed in the concrete layer, and the MCNP6 f4 track length flux tally is used to compute neutrons and photons average flux. In Figure 5.1 the 10 detectors can be observed. In the figure, the proton beam runs horizontally.

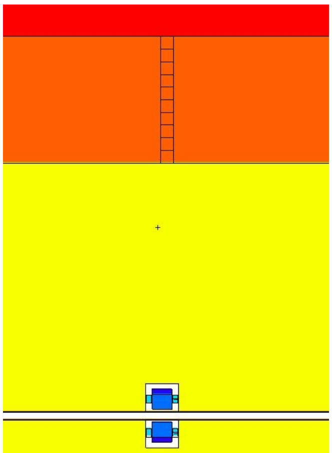

Figure 5.1: detectors in the concrete layer (beam tube in white, air in yellow, concrete in red).

In order to speed up the calculation, the weight windows variance reduction technique has been implemented. The weight windows have been generated for a 1D mesh, refined in the detectors' direction. The basic idea is to push particles towards the last detector (the closest to the concrete external surface). To do this, an iterative process has been implemented, generating weight windows for the detector closest to the inner concrete surface in the first run, and progressively changing the tally location to further detectors, until the last one is reached.
The first simulation was performed by using the conservative simplifying assumption of protons emitted all at the same energy of 17 MeV from the source. The detectors have been placed in correspondence of half-length of the beam line.
In the second simulation, the fact that not all the protons are lost from the beam at the same energy has been considered. In order to get the most conservative result for this case, the axial position of the 10 detectors has been changed from the middle to the end of the tunnel, in correspondence of the section in which protons are lost at 17 MeV. Moreover, since protons are lost with a certain angle (defined in the source card), also the particles coming at lower energies from previous locations along the beam axis will reach the detectors. Because of that, the dose rates are expected to be lower with respect to the previous case, in which all the particles reaching the tally had been generated by the interaction of protons all at the same energy with the beam tube.
Results for neutrons and photons dose rates are plotted in Figure 5.2-top and Figure 5.2-middle. As expected, the values obtained in the second simulation (considering protons lost at different energies) are always smaller than the ones of the first simulation (all protons lost at 17 MeV).
In Figure 5.2-bottom, the total dose rate is shown for both cases. Even though the dose rate at the end of the concrete shield is a little bit above the limit in the most conservative simulation, these results show that the limit is respected in the most realistic case.
In all the plots, the vertical bars represent statistical uncertainties. The maximum relative error is 11 % for the results related to neutrons, and 15 % for photons. Statistics could be improved, trying to reach an error below 10 % everywhere, but it is already like that in most of the cells that where tallied and, most importantly, in the last cell (further from the beam line), which is the one that is used to compare to the limit.

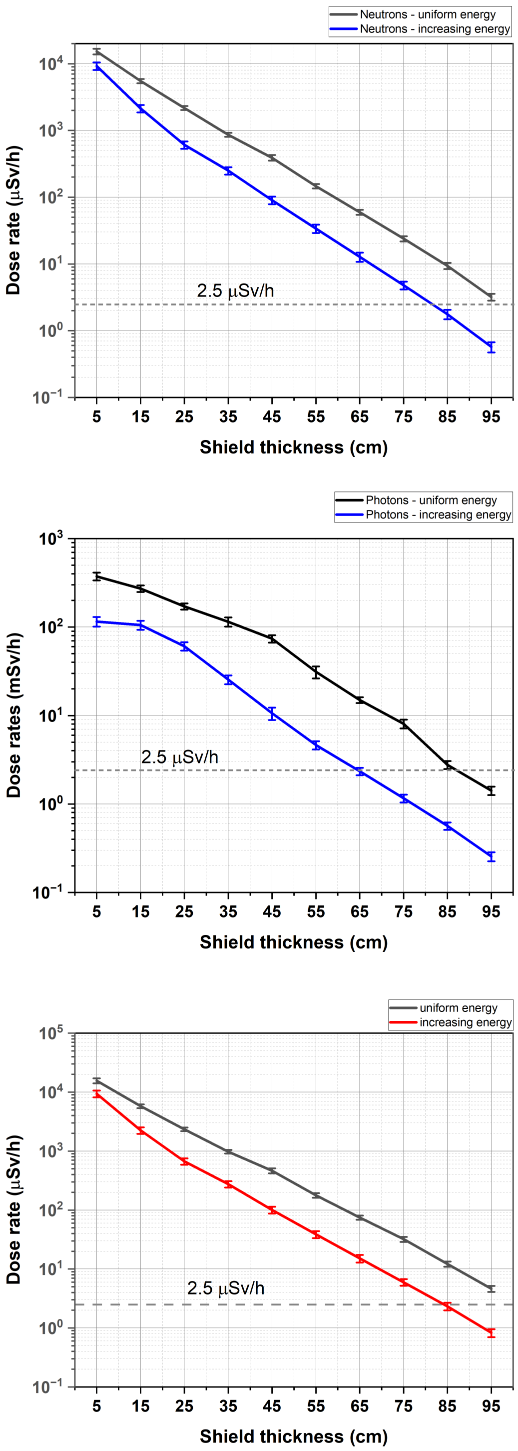

Figure 5.2: neutrons (top), photons (middle) and total (bottom) dose rates as function of the shield thickness.

5.2 Lighting fixtures

Lighting fixtures will be present on the injector tunnel ceiling. The cumulative dose in these components must be determined in order to understand if they will withstand long irradiation periods or if a replacement strategy has to be considered. The limit of cumulative dose for conventional lighting fixtures is about 10 Gy. If this limit is exceeded, the materials may experience radiation hardening and the lighting fixtures will need to be replaced more often. In this case, radiation hardening resistant lighting fixtures should be considered. Producers can provide different types of fixtures, depending on the amount of accumulated dose (< 50 kGy, 50 kGy > x > 500 kGy, > 500 kGy).
The lighting fixtures are composed of the following components (and materials):

1. Fe+Zn coating ($90\% Fe, 10\% Zn$);
2. Copper (Pure Cu);
3. Aluminium (Standard industrial $Al6061$);
4. Electronics (Si);
5. Stainless Steel (AISI 304).

The aim of this simulation is to estimate what is the order of magnitude of the accumulated dose in the five different materials that compose the lighting fixtures. Since modeling the actual geometry of a lighting fixture may be complex and not very relevant for the purpose of this work (which is to determine a range for the value of the accumulated dose), a simplified scheme has been implemented. The five different components have been studied separately and modeled as little rectangular boxes, placed at middle length (in correspondence of the 10 MeV region) and at the end of the tunnel (17 MeV), on the ceiling. As far as the dimension of the boxes is concerned, two configurations have been studied:

1. 10 cm x 10 cm base, 10 cm height;
2. 10 cm x 10 cm base, 1 cm height;

The two geometrical configurations are shown in Figure 5.3.

In order to compute the accumulated dose in Gy/y, the $f6$ MCNP6 tally has been used. The $f6$ tally provides the energy deposited in the detector in MeV/g, normalized to the source particles (protons). Thus, the result has been multiplied by the number of protons/s and converted to Gy/y.
The results are collected in Table 5.1 and Table 5.2 for the first configuration; in

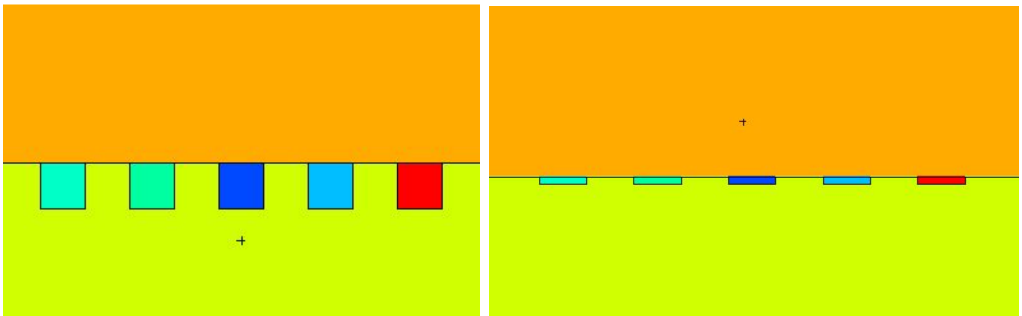

Figure 5.3: Geometrical configuration for two simplified models of the lighting fictures: 10cm x 10cm x 10cm on the left, 10cm x 10cm x 1cm on the right.

Table 5.3 and Table 5.4 for the second one. The relative error for these results is below 10 %.
In all the cases that have been analyzed, the limit of 10 Gy is reached after approximately 10 years. After the operational life period of the injector of 40 years, the absorbed dose is several times greater than this limit, but it is still way below the limit of 50 kGy. This means that, if the correct device is chosen, no replacement due to irradiation hardening is foreseen.

Table 5.1: Absorbed dose for lighting fixtures in the 10 MeV region, dimensions 10cm x 10cm x 10cm. Relative error < 10%.

Material	**[Gy/y] - 10 MeV**	**[Gy/10y] - 10 MeV**	**[Gy/40y] - 10 MeV**
Fe+Zr	1.11	11.1	44.6
Cu	1.78	17.8	71.3
Al 6061	1.15	11.5	46.1
Si	0.92	9.21	36.9
AISI 304	1.43	14.3	57.0

Table 5.2: Absorbed dose for lighting fixtures in the 17 MeV region, dimensions 10cm x 10cm x 10cm. Relative error < 10%.

Material	[Gy/y] - 17 MeV	[Gy/10y] - 17 MeV	[Gy/40y] - 17 MeV
Fe+Zr	3.52	35.2	141
Cu	4.1	41.0	164
Al 6061	3.22	32.2	129
Si	3.42	34.2	137
AISI 304	2.83	28.3	113

Table 5.3: Absorbed dose for lighting fixtures in the 10 MeV region, dimensions 10cm x 10cm x 1cm. Relative error < 10%.

Material	[Gy/y] - 10 MeV	[Gy/10y] - 10 MeV	[Gy/40y] - 10 MeV
Fe+Zr	1.59	15.9	63.4
Cu	2.23	22.3	89.3
Al 6061	1.18	11.8	47.4
Si	0.933	9.33	37.3
AISI 304	1.84	18.4	73.5

Table 5.4: Absorbed dose for lighting fixtures in the 17 MeV region, dimensions 10cm x 10cm x 1cm. Relative error < 10%.

Material	[Gy/y] - 17 MeV	[Gy/10y] - 17 MeV	[Gy/40y] - 17 MeV
Fe+Zr	5.05	50.5	202
Cu	5.4	54.0	216
Al 6061	4.3	43	172
Si	4.04	40.4	161
AISI 304	4.23	42.3	169

5.3 Injector entrance without shielded door

Dose rates due to the prompt radiation from the injector must be determined in the injector access area. The entrance will have the shape of a rectangular room, right next to the injector tunnel wall. In Figure 5.4, the drawing of the access room is shown. The reference point for dose rate calculation is represented in yellow. The objective of this work is to verify that the dose rate in the reference point is compliant with the supervised area limit of 0.75 μSv/h.

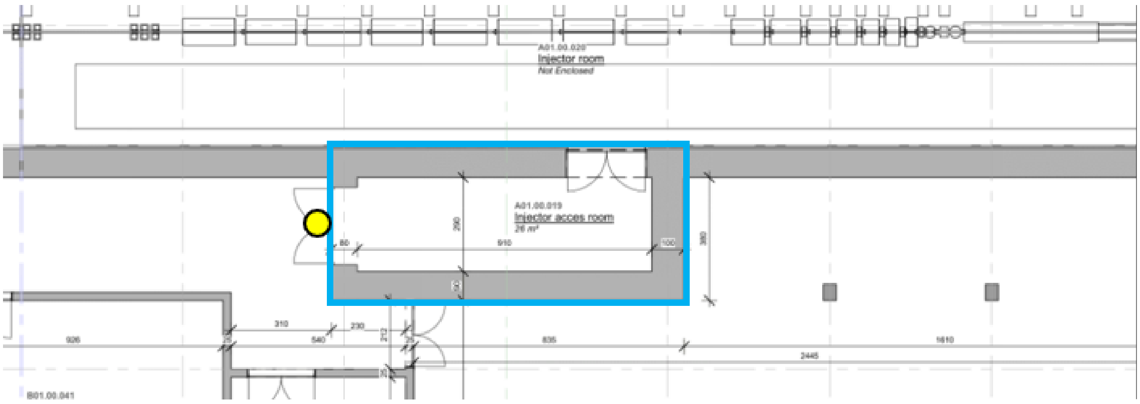

Figure 5.4: injector access room. Reference point in yellow.

At the beginning of this work, a preliminary design was proposed for the injector entrance. After some time, the design was changed due to space management reasons in the injector building. In this sub-chapter, the results for both designs are presented and the main differences highlighted.
From a methodology point of view, in both cases dose rate maps have been produced for the whole injector and entrance, on the basis of a mesh defined in a *fmesh* tally.
To speed up calculations, the weight windows variance reduction technique has been coupled to DXTRAN spheres. In particular, two communicating DXTRAN spheres have been defined at both doors of the entrance room. Using two spheres is much more useful, since the particles scattered from the first sphere will be directed to the second one.

5.3.1 First design

The first proposed design is presented in Figure 5.5. In Figure 5.6, the MCNP model and the location of the DXTRAN spheres are shown.

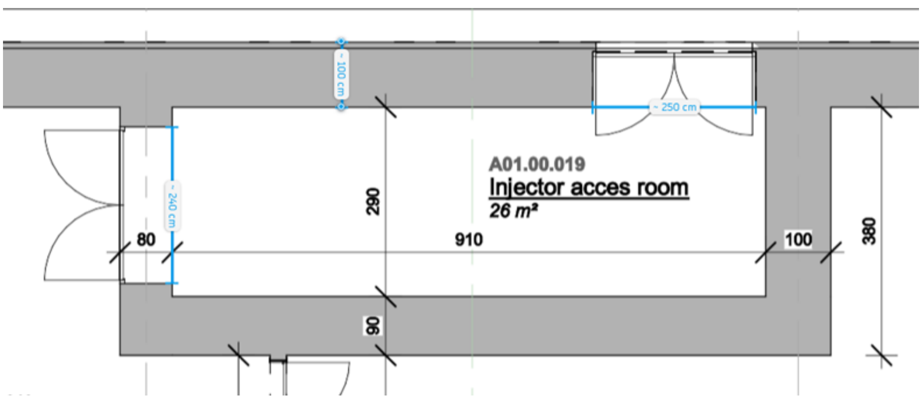

Figure 5.5: first design dimensions.

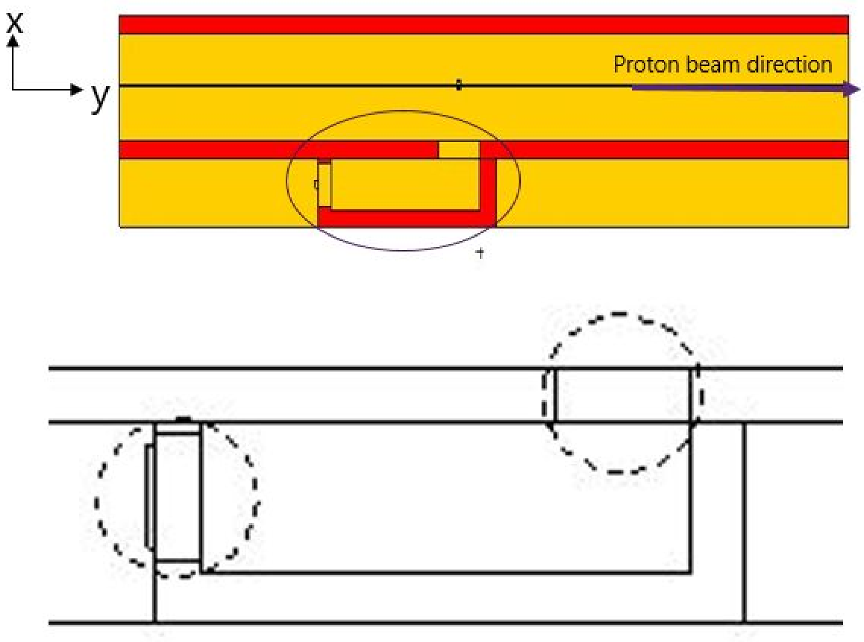

Figure 5.6: MCNP model of the first design and DXTRAN spheres location.

In Figure 5.7, the total dose rate map of the injector and of the access room are represented. In Figure 5.8, the maximum dose rate profile along the y direction (z=0, x=−588 cm) and along the x-direction (z=0, y=279.68 cm) are plotted.

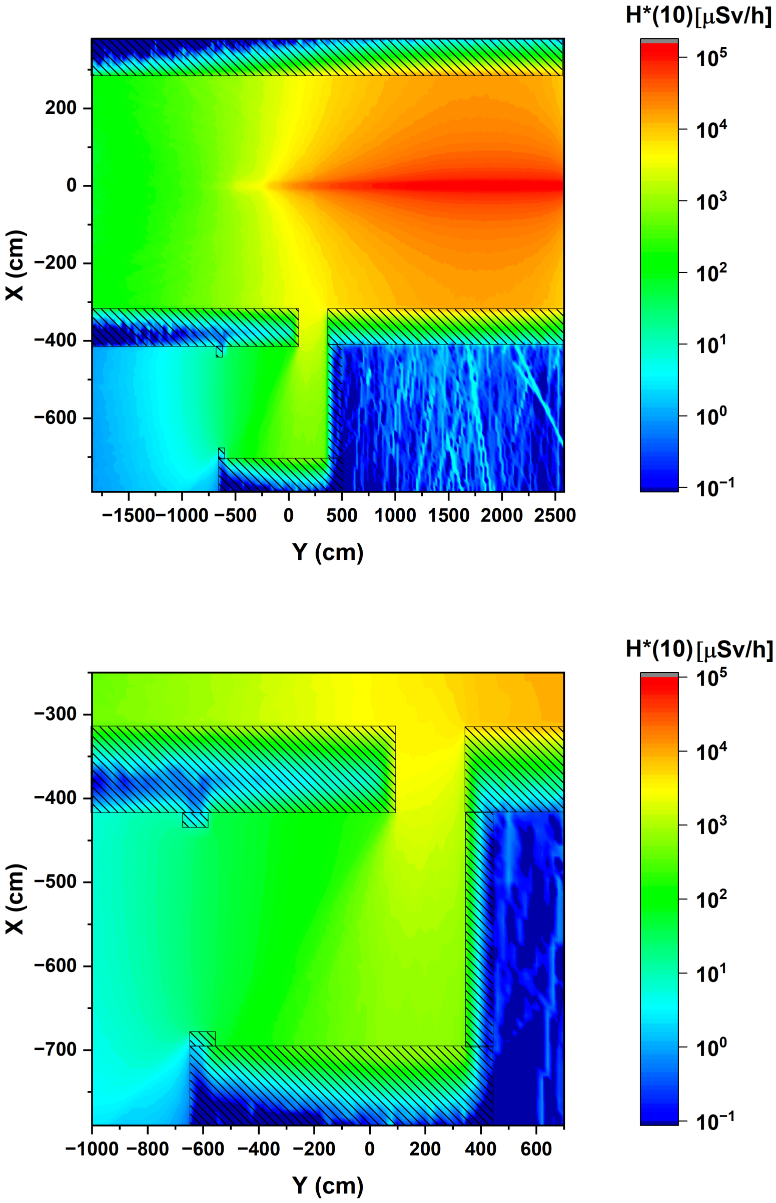

Figure 5.7: Total dose rate map (top). Detailed dose rate map at the entrance (bottom).

In both directions, attenuation in the concrete wall can be observed. In the x-direction, the position of the wall helps in reducing the total dose rate to a very low value, which means that concrete is effective in shielding the external

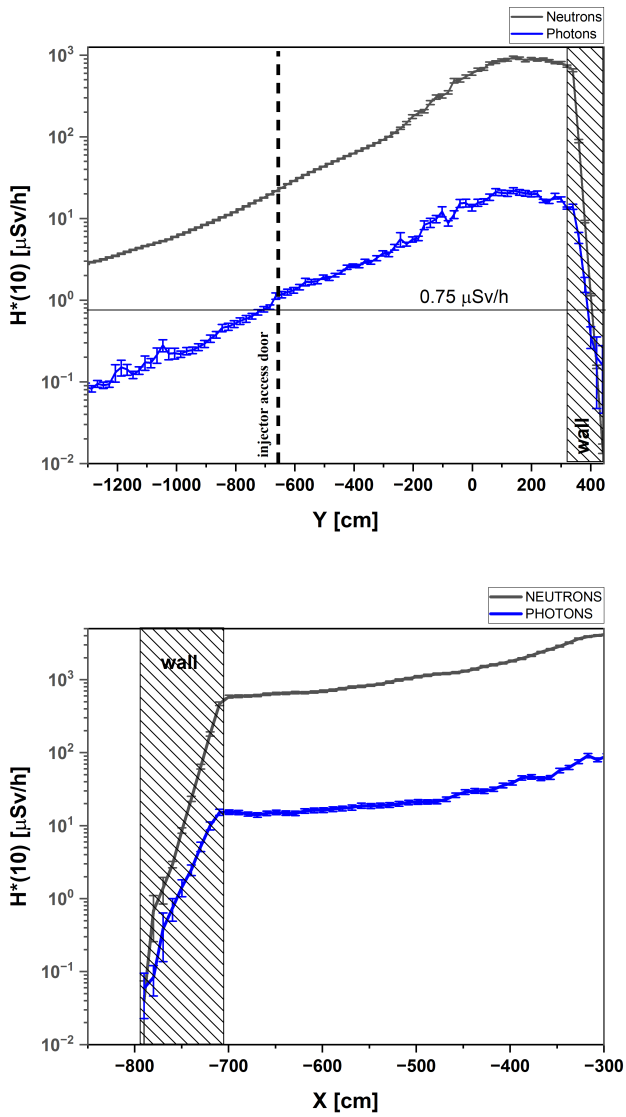

Figure 5.8: Dose rate profile along the y direction (z=0, x=−588 cm) (top) and along the x direction (z=0, y=279.68 cm) (bottom).

environment from the radiation generated inside the injector tunnel.
newpage On the contrary, in the y-direction, the dose rate remains relatively high in the area of interest (injector access door) because of the absence of a shielding door. In fact, the decrease of both neutrons and photons dose rates is only due to attenuation in air, which of course is not enough.
The dose rate at the access door due to neutrons is 23.97 ± 0.24 μSv/h, while for photons is 1.09 ± 0.11 μSv/h. The total dose rate is equal to 25.08 ± 0.35 μSv/h, which is way above the limit of 0.75 μSv/h.

5.3.2 Second design

The second design, which is shown in Figure 5.9 (top), is quite similar to the first one, with a major change in the dimensions. Another major change is in the orientation of the room, which is now in the opposite direction, as in Figure 5.9 (bottom). On the basis of these two modifications, the dose rates at the door are

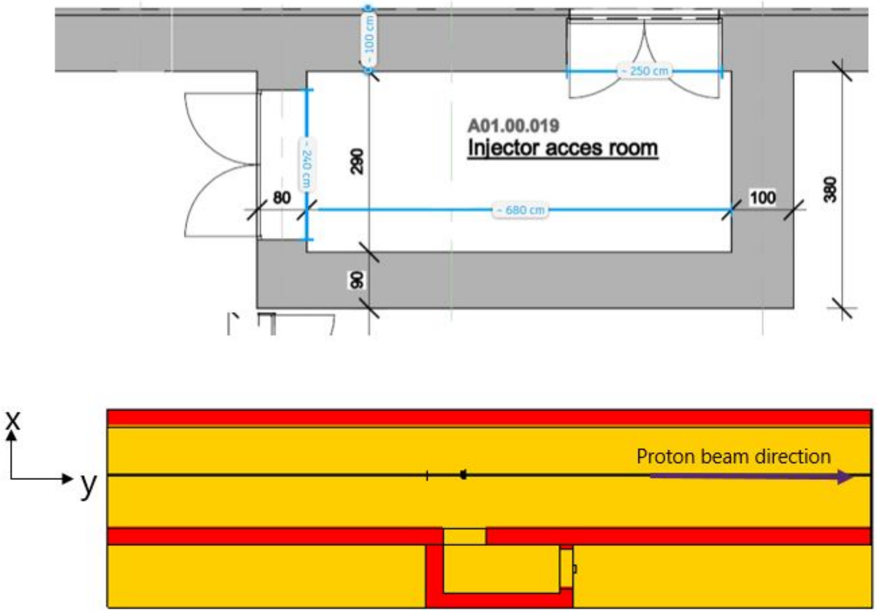

Figure 5.9: Second design dimensions (top). MCNP model of the second design (bottom).

expected to be greater than the previous case. The two main reasons are that, being the length of the room smaller, the door is closer to the injector tunnel, and that the proton beam is directed in the same direction of the door.
In Figure 5.10, the dose rate maps are shown, while maximum dose rate profile in y and x directions are plotted in Figure 5.11.
Also in this case, as in the previous one, both photons and neutrons experience the major attenuation in the concrete wall, which is an effective shield for the dose rate in the x direction. On the other hand, in the y direction, only air attenuation is possible, and the dose rates remain high.
As expected, the limit for the supervised area is exceeded, since the contribution coming from neutrons and photons is of 38.51 ± 0.47 μSv/h and 1.73 ± 0.12 μSv/h, respectively. The total dose rate at the entrance door is 40.24 ± 0.58 μSv/h.

On the basis of these results, a shielded door is needed in order to reduce the dose rate at the access door.

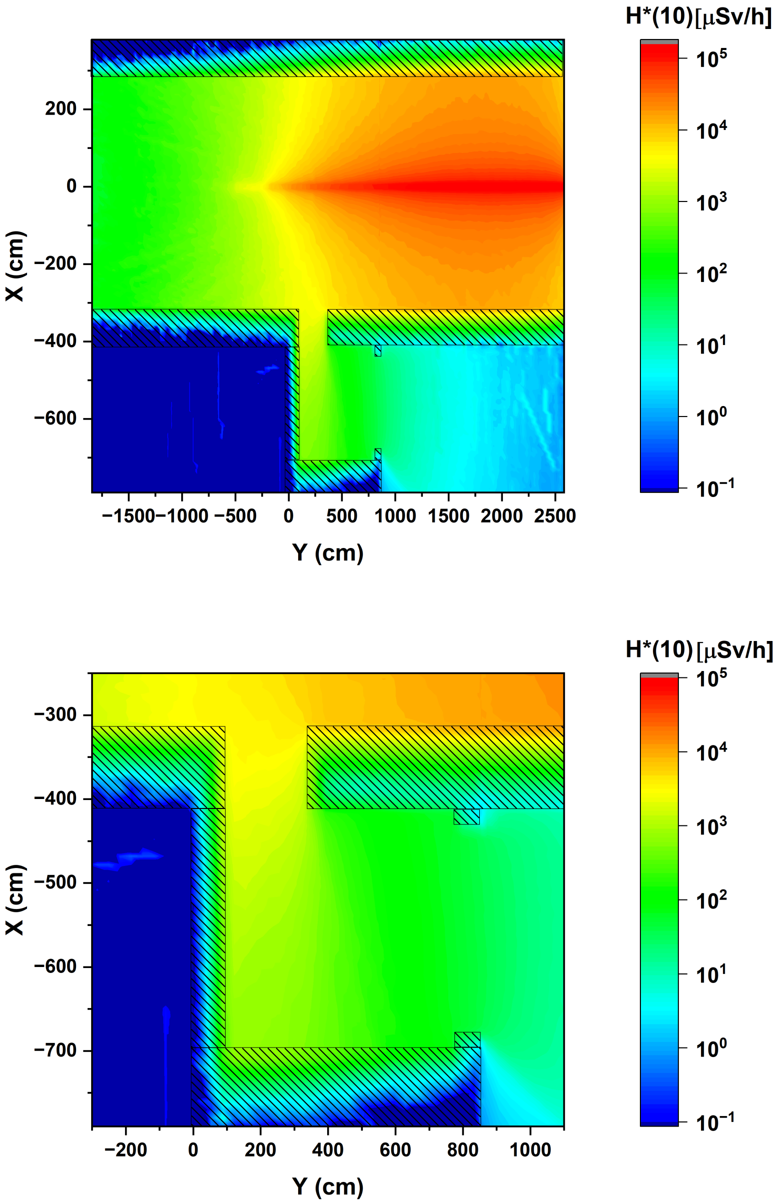

Figure 5.10: Total dose rate map (top). Detailed dose rate map at the entrance (bottom).

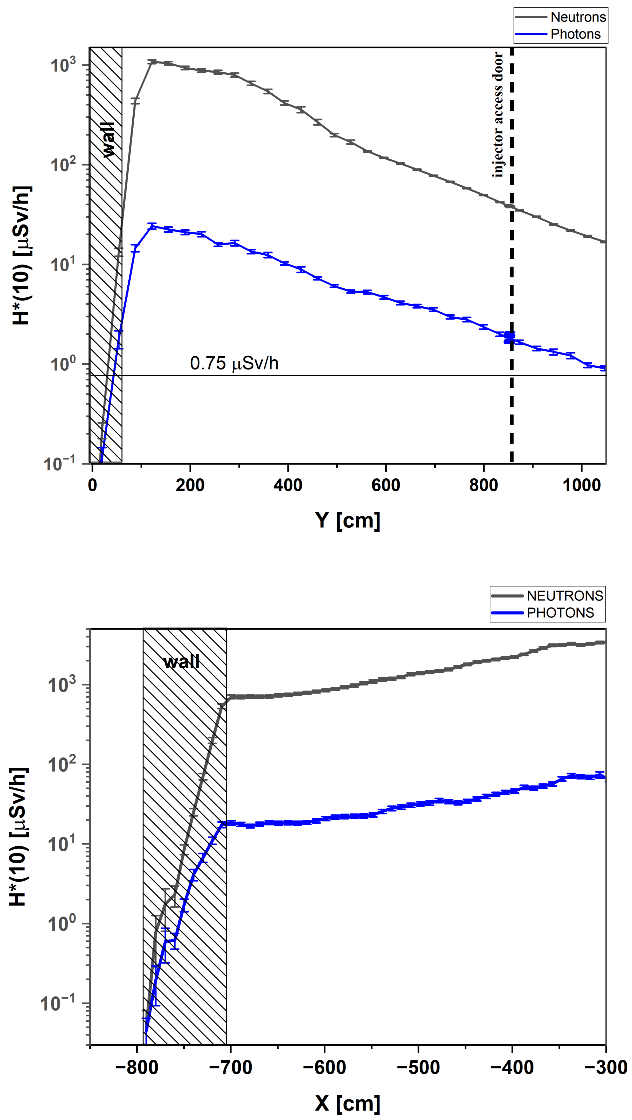

Figure 5.11: Dose rate profile along the y direction (z=0, x=−588 cm) (top) and x direction (z=0, y=279.68 cm) (bottom).

In Figure 5.12 spectra for neutrons and photons are presented. Information about the spectrum can be very useful in the design stage of the shielding door, since the attenuation coefficient also depends on the particles' energy.

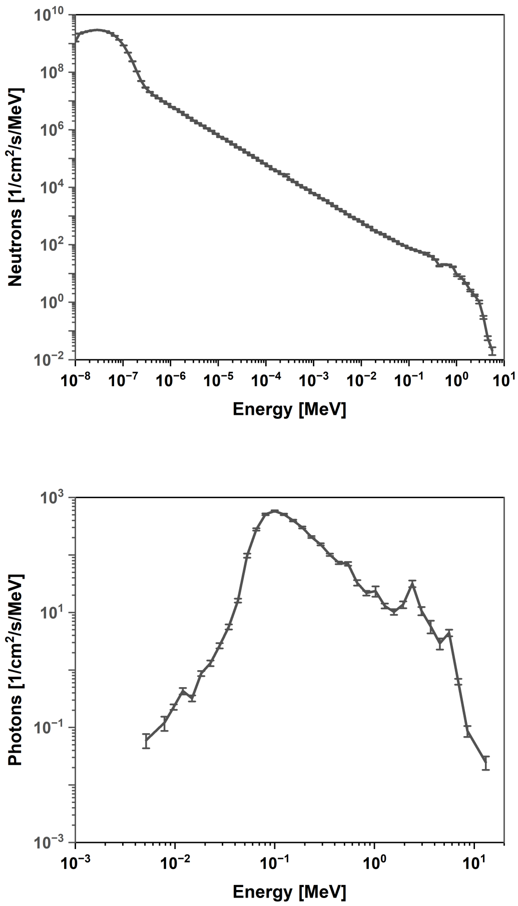

Figure 5.12: Neutrons spectrum at the access door (top). Photons spectrum at the access door (bottom)

5.4 Shielded door design

5.4.1 Neutron and photon shielding

One of the main concerns in the design of nuclear facilities is neutron shielding. In fact, when compared to the same dose of γ or x-rays, neutrons can lead to much more harm in the human body. Nevertheless, also the effect of photons may be relevant. In particular, secondary photons will form due to the interaction of neutrons with the shielding material. In general, the shielding performance is determined by the incident particles' energy, the shielding material and the size of the shield [23].
Practically, three steps are usually considered in the design: neutrons slowing down, neutrons absorption and γ shielding.
Hydrogenous materials can be used to effectively slow down neutrons to thermal energies [24]. For very fast neutrons, iron or lead can be placed in front of the hydrogenous material. The slowing down process in hydrogenous materials is mainly driven by elastic scattering with hydrogen, which leads to large neutron energy loss due to the relative small mass of hydrogen [25]. Moreover, this type of material is also quite effective at absorbing neutrons. The main drawback is that a difficult to shield 2.2 MeV photon is emitted when a neutron is absorbed by hydrogen [26].
In industrial applications, polyethylene (PE) is widely used due to its high hydrogen content. Sometimes, its performances are improved by adding a certain quantity of boron (BPE), which has a large absorption cross section and only emits a low energy photon. Polyethylene and boron carbide are mixed evenly through high speed stirring. The resulting mixture is plasticized and prepared by pressure modelling, obtaining the final BPE shielding material [27].
The layer of PE or BPE can be then be coated by layers of steel on both sides. Steel is used to shield secondary photons that will eventually be produced in the neutron shielding phase. Moreover, the presence of steel can also improve the structural stability of the door.
Another option is to couple PE or BPE with an high Z material, such as lead, which is particularly effective at shielding photons. On the other hand, when compared to low Z materials, the high Z ones get more activated by neutrons.

5.4.2 Preliminary simulations

In order to understand how neutron attenuation works in different materials, some preliminary simulations have been performed. In these models relatively thin layers of 5 cm PE or BPE (polyethlene with 10 % boron) and 2 mm steel have been studied. In Figure 5.13, a comparison between the neutron shielding performance of PE and BPE is shown. As expected, BPE is much more effective at shielding neutrons due to the presence of boron. In these results, only the contribution of neutrons to the dose rate is presented, since it is already much above the limit of 0.75 μSv/h, being 8.33 μSv/h and 6.55 μSv/h for PE and BPE, respectively. As a consequence of these numerical results, the preliminary model with 5 cm thickness is definitely not enough for the purpose of this work, and thicker layers must be considered.

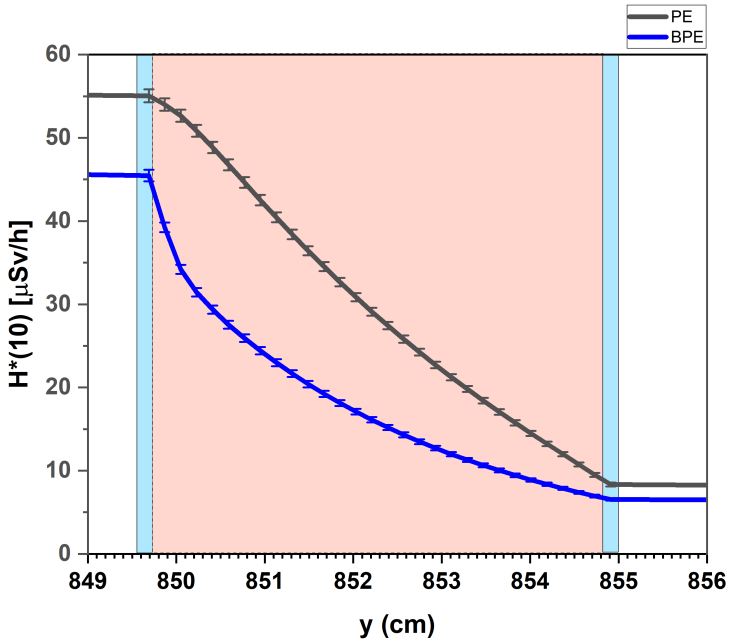

Figure 5.13: comparison of the neutron dose rate contribution for polyethylene and borated polyethylene.

5.4.3 Theorethical considerations

Neutron attenuation in a medium follows the exponential attenuation law:

$$I(d) = I_0 exp(-\Sigma_r d) \tag{5.1}$$

where $I(d)$ is the neutron fluence rate (or dose equivalent rate) in neutrons/(cm^{2}s), d is the shielding thickness in cm, and Σ_r is the neutron removal cross section in cm^{-1}.
On the basis of the results of the preliminary simulations, the removal cross section for neutrons can be estimated. Considering a shielding thickness of 5 cm and the numerical values presented in the previous section, the estimated removal cross sections are about 0.38 cm^{-1} for PE and 0.39 cm^{-1} for BPE. Using these numbers, at least 12 cm of PE or 11 cm of BPE are needed to reduce the neutron dose to 0.75 μSv/h. Of course, this would still not be enough to properly shield the entrance room, because of the contribution coming from photons. For this reason, a thickness of 15 cm will be considered for the successive calculations.
For photon attenuation, the linear attenuation coefficient is usually considered. This parameter is strongly dependent on the photon energy. According to the spectrum in Figure 5.12, there is a peak of photons at 0.1 MeV. At this energy, the linear attenuation coefficient for lead is at one order of magnitude greater than the one for stainless steel [28] [29]. As a consequence of that, lead is expected to be more effective in the shielding of photons, and can be considered in case the steel performance is not good enough.

5.4.4 Proposed designs

In this sub-chapter, two design proposals for the shielded door are presented. In both cases, a central layer of BPE (polyethylene with 10 % boron) of 15 cm is present. In the first design, BPE is coated with 1 cm of steel on each side. In the second one, lead is used instead of steel.
The total dose rate maps, maximum dose rate profile along the y-direction and the dose rate at the door are shown in Figure 5.15 and Figure 5.16, for the first and second design, respectively.
In Figure 5.14, a comparison of the total dose rates for the two configurations is plotted.
The results show that the first design is not enough to effectively shield and reduce the dose rate at the reference point below the limit of the supervised area. In fact, even if a relevant reduction can be observed at the door, the total dose rate is still 1.57 ± 0.15 μSv/h, about the double of the objective. This relatively high dose is due the contribution of photons, which do not experience a sufficient attenuation in the steel layers.

On the contrary, the second design is enough to reach the desired value, since the total dose rate at the door is 0.67 ± 0.08 μSv/h. In fact, as expected, lead is a much better shielding material for photons, and a greater attenuation can be observed in it.
In both cases, the photon attenuation is more relevant in the outer layers, while the photon dose rate experience only a small decrease in the BPE. Moreover, a local increase of the dose rate can be observed at the beginning of the BPE. This can be explained considering that photons are emitted due to the interaction of neutrons with BPE.

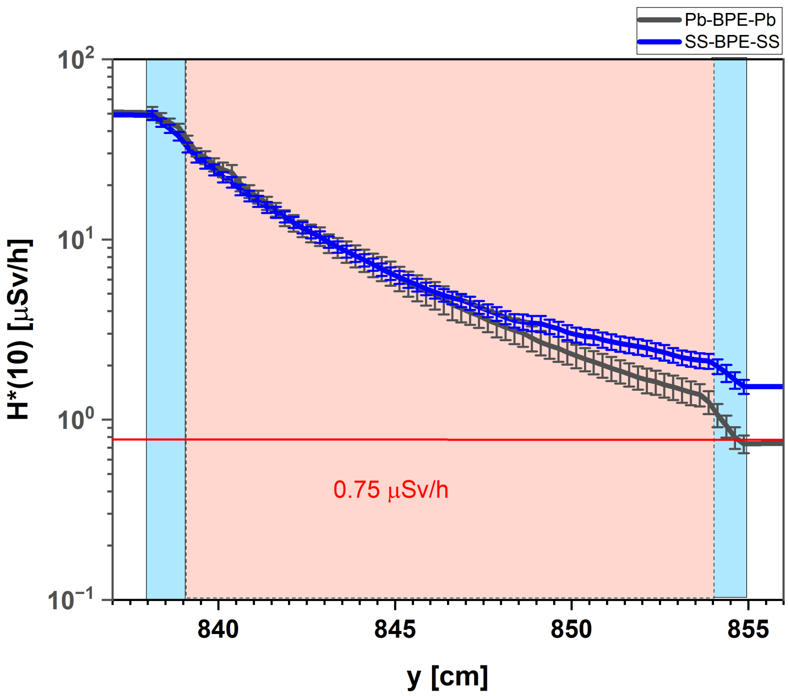

Figure 5.14: Comparison between total dose rate profiles for steel-BPE-steel and Pb-BPE-Pb

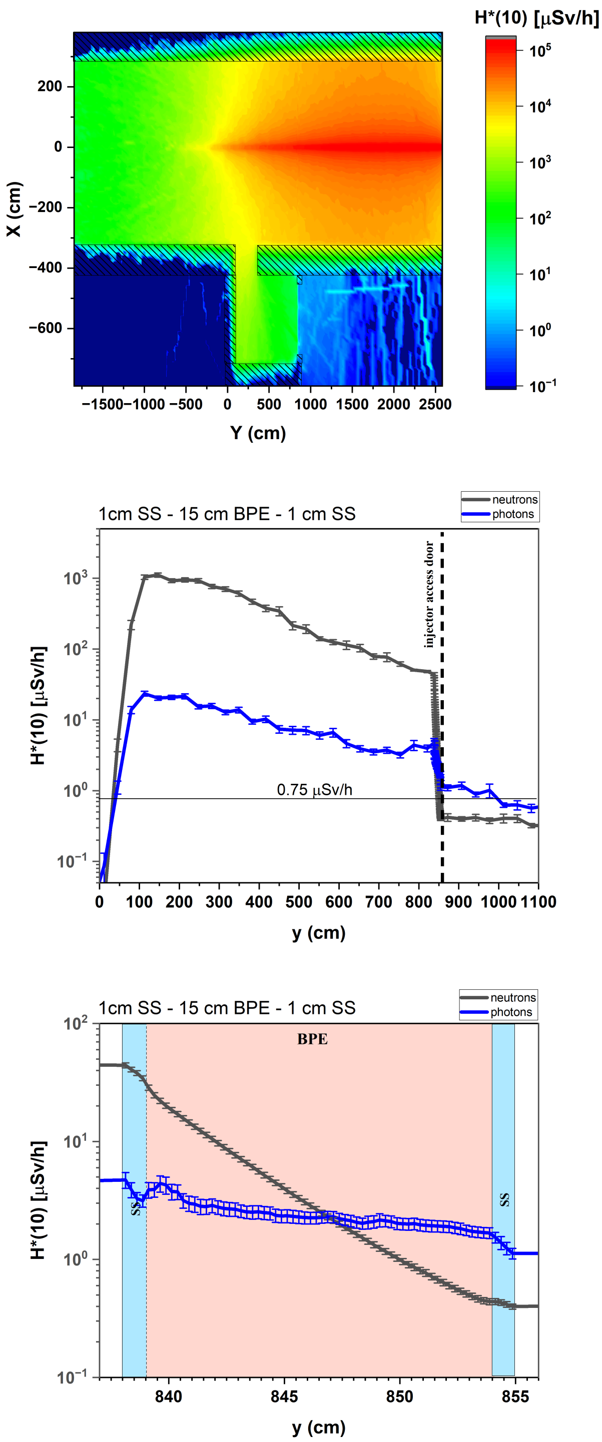

Figure 5.15: Results for the steel-BPE-steel configuration. Dose rate map (top). Dose rate profile along the y direction (z=0, x=−558 cm) (middle). Dose rate profile at the shielding door (bottom)

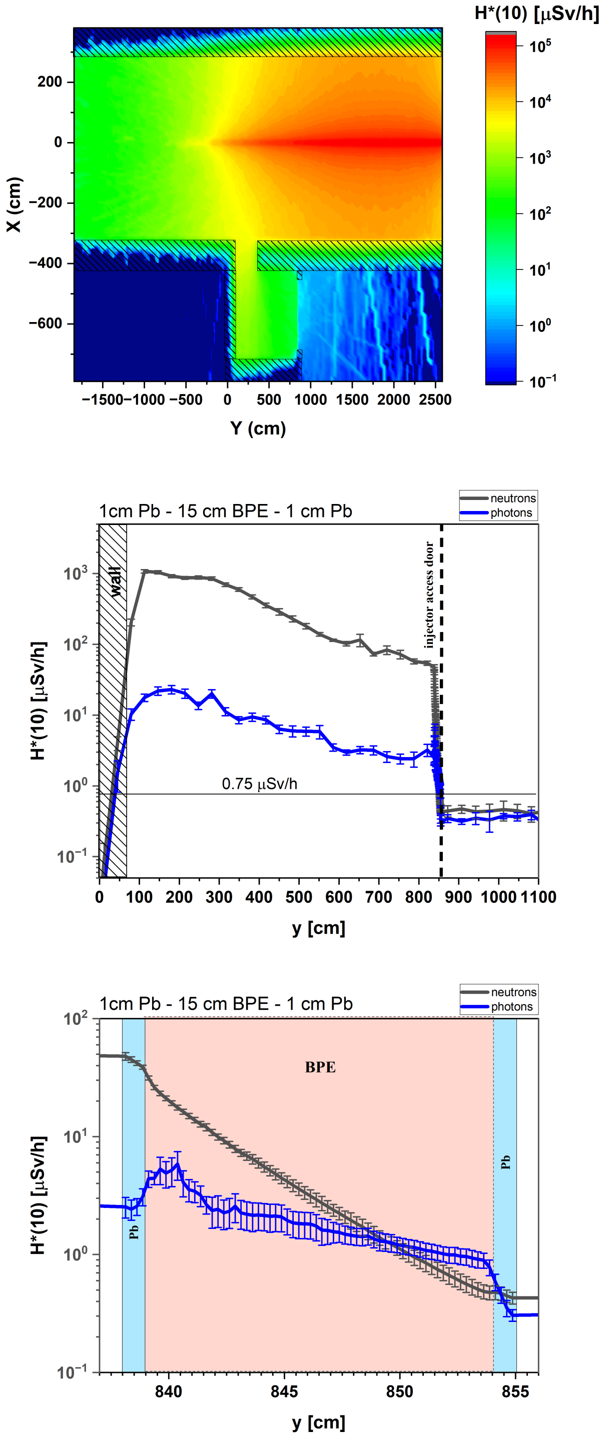

Figure 5.16: Results for the Pb-BPE-Pb configuration. Dose rate map (top). Dose rate profile along the y direction (z=0, x=−558 cm) (middle). Dose rate profile at the shielding door (bottom)

In Table 5.5, a summary of the main results obtained in this section is presented. The maximum relative error is 12 %, and it is related to the Pb-BPE-Pb configuration. For the other cases the error is below 10 %.

Table 5.5: Neutrons, photons and total dose rates for the injector entrance: comparison between configuration without shielding door and the two analysed designs. Relative error $\leq$ 12%.

	Neutrons [μSv/h]	**Photons [μSv/h]**	**Total [μSv/h]**
Without door	38.5	1.7	**40.2**
steel-BPE-steel	0.39	1.18	**1.57**
Pb-BPE-Pb	0.38	0.29	**0.67**

In conclusion, the three-layers design with lead and BPE is the best choice among the ones that have been analysed in this work (since it is the only configuration that respect the limit). The objective was reached thanks to a balance in the contributions of photons and neutrons to the total dose rate. By changing the relative contributions, also other configurations may be considered. As an example, the fact that relatively thin (when compared to the thickness of BPE) layers of Pb are needed to effectively attenuate photons may be exploited in order to reduce the total thickness of the shielding door.

5.5 Beam dump prompt radiation shielding

For the beam dump, a shielding design has already been proposed by SCK CEN. It is represented in Figure 5.17. The beam dump is positioned behind the wall of the injector tunnel. The injector wall shall be part of the shielding of the beam dump, as this is place efficient. This results in a total shielding thickness of 2.50 m in forward and backward direction, and 2.30 m in lateral direction. Standard concrete is assumed as shielding material.

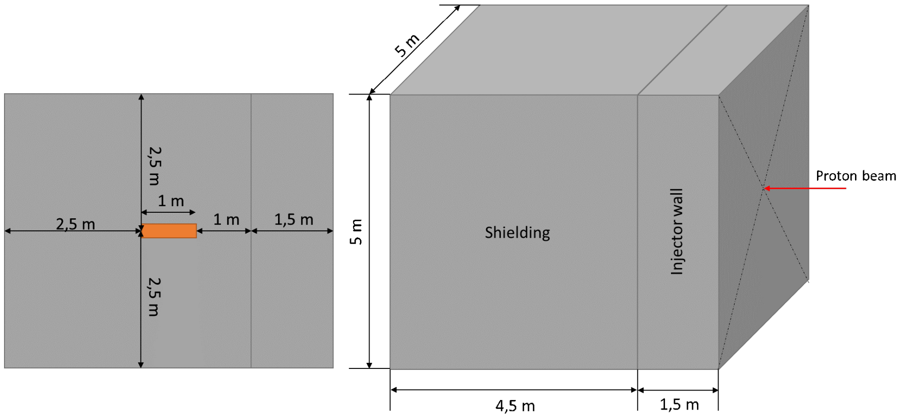

Figure 5.17: Beam dump shielding concept

The objective is to verify that this configuration permits a sufficient reduction of the prompt dose rate in forward, backward and lateral directions, in compliance with the limit of the supervised and controlled areas, as shown in Figure 5.18.

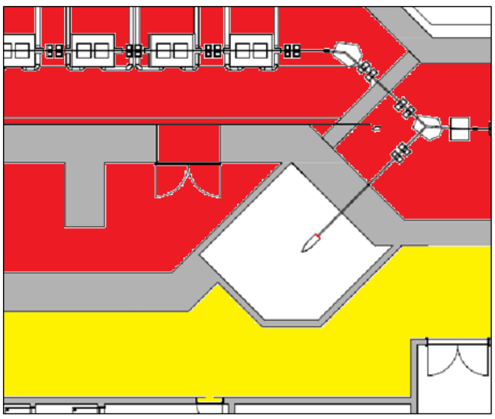

Figure 5.18: Dose rate limits zoning: supervised area in yellow (0.75 μSv/h); controlled area in red (2.5 μSv/h).

In order to study the attenuation in the concrete shield, detectors have been placed in the three directions that need to be studied. Each direction has been analysed in a separate simulation. Also in this case, weight windows based on a 1D mesh have been used.
The reference source configuration, for this case, is the reduced duty-cycle, that has been described in Chapter 4. This means that an average 0.3 mA proton current at 17 MeV hits the beam dump. In the worst case scenario, the reduced duty cycle may not be feasible, and a full duty cycle will be used.
In Figure 5.19 and Figure 5.20, the detectors and the dose rate attenuation for reduced and full duty cycle is shown, for forward and lateral direction.

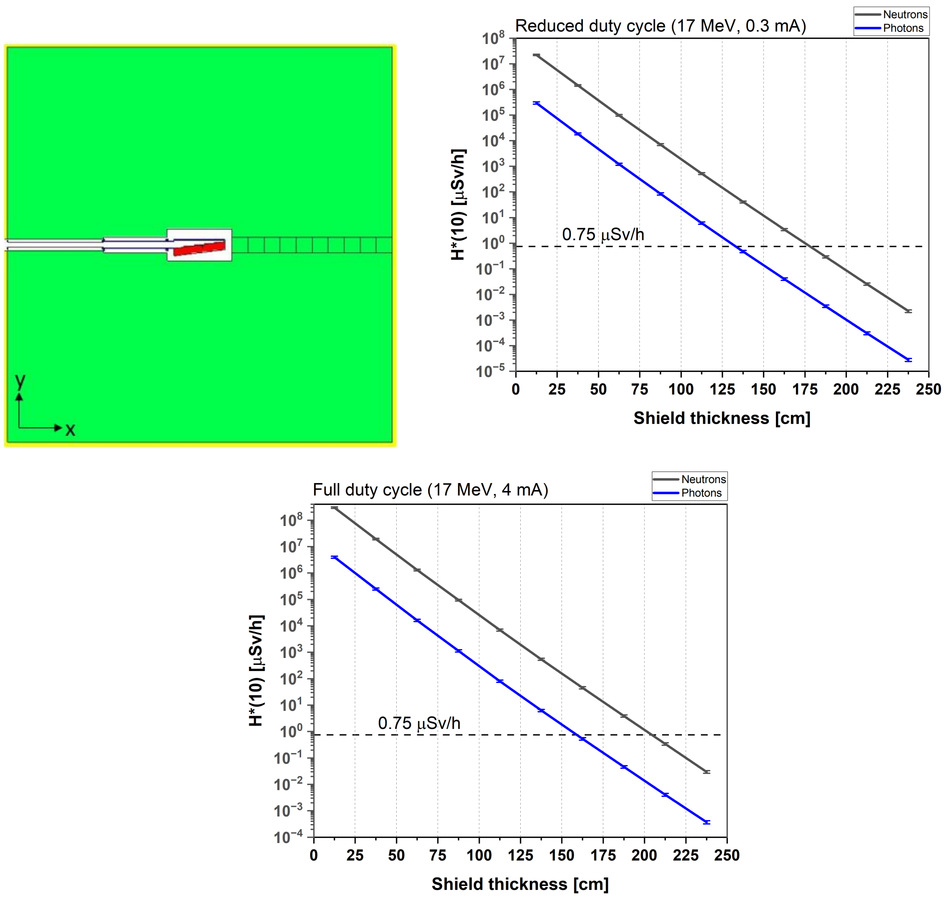

Figure 5.19: Dose rates in forward direction. Detectors (top, left). Results for reduced duty cycle (top, right) and full duty cycle (bottom).

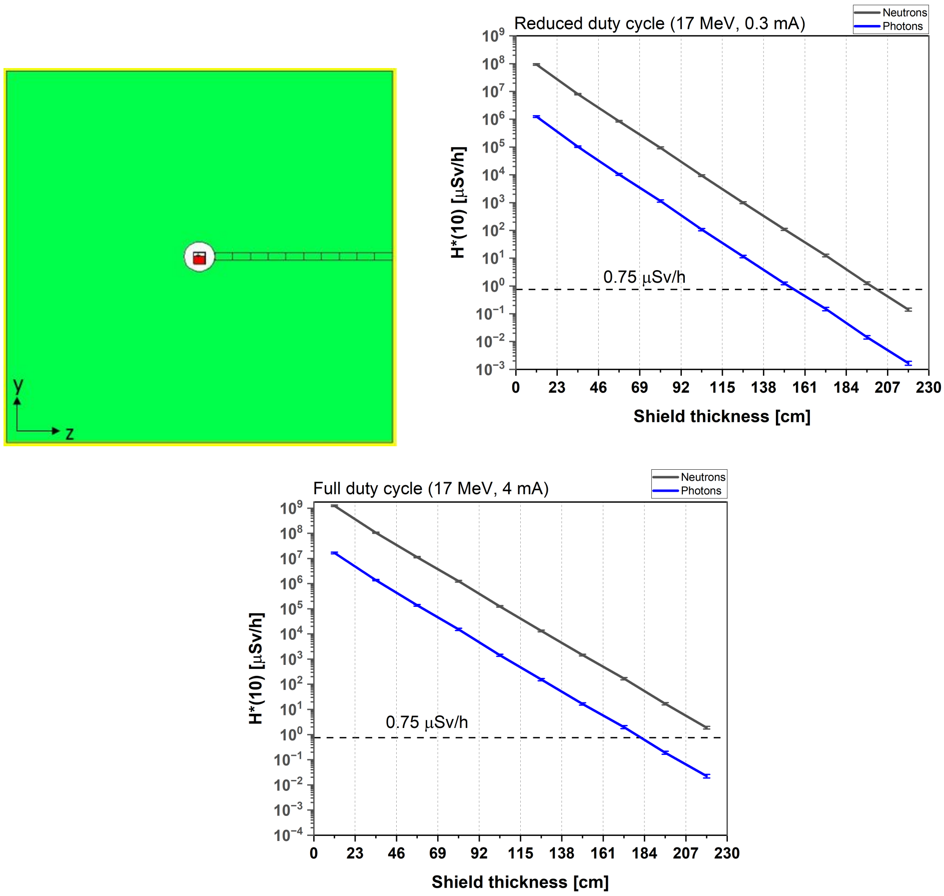

Figure 5.20: Dose rates in lateral direction. Detectors (top, left). Results for reduced duty cycle (top, right) and full duty cycle (bottom).

As far as the reduced duty cycle is concerned, the limit is reached after about 2.0 m, in both cases. The additional space permits to reach very low doses. In the furthest detectors, the total dose rates (sum of the neutrons and photons contributions) are 0.0023 ± 0.0003 μSv/h and 0.1602 ± 0.0184 μSv/h, respectively for forward and lateral directions.
On the other hand, with the full duty cycle, the shielding requirement is verified only in the forward direction, where in the last detector the dose rate is 0.030 ± 0.003 μSv/h, while it is above the limit in the lateral one, being it 2.140 ± 0.241 μSv/h. It should be noticed that this number is even greater than the limit for the controlled area. Thus, an increase of the shielding thickness may be useful, in order to comply with the safety requirements, even in case of full duty cycle.
In backward direction, detectors have been placed a bit further from the axis of the cube, since dose rates are expected to be very high next to the void tube. This case

is actually reported for completeness, and gives an idea of the attenuation in this layer, but it is not of practical interest, since no-one will enter the injector tunnel while the beam is on. In any case, the limit for the controlled area in satisfied with the reduced duty cycle, but not with the full one.

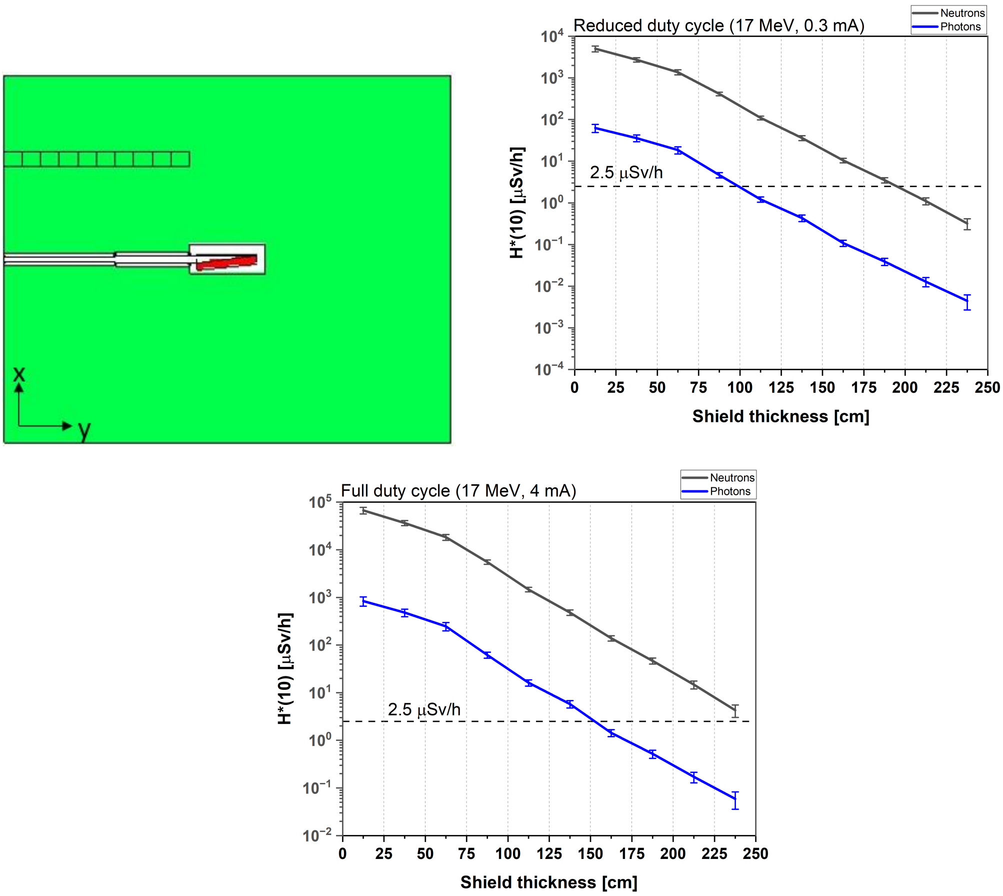

Figure 5.21: Dose rates in backward direction. Detectors (top, left). Results for reduced duty cycle (top, right) and full duty cycle (bottom).

5.6 Beam dump activation and residual radiation

In order to calculate the activation of the materials constituting the beam dump and the surrounding shield, the irradiation history must be considered. Of course, the beam dump will not be used continuously for 40 y (the operational life of the accelerator), because there will be periods of maintenance, stand-by, etc. Moreover, when the facility will be updated to MYRRHA, two injectors and two beam dumps (one per each injector) will be present. One injector will feed the reactor, while the other one will be in stand-by, which means that the beam will be directed towards its own dump.
Two cases are analysed in this thesis: 5 years of MINERVA operation by its own, followed by 35 years of MYRRHA operation; and, for completeness, 40 years of MINERVA operation, in case there will be no upgrade to MYRRHA.
SCK CEN project engineers have estimated a total of 4976.4250 working days for the first case and 730.4844 days for the second, in reduced duty cycle.
The activation of the CuCrZr beam dump core and of the adjacent layers of concrete has been calculated. In order to understand the difference in the activation of the concrete in the different directions, three volumes have been selected (forward, backward and lateral directions), as shown in Figure 5.22.
In Figure 5.23, the specific activity for beam dump core and the concrete layers is plotted for both irradiation configurations. A decay period of 25 days is considered.

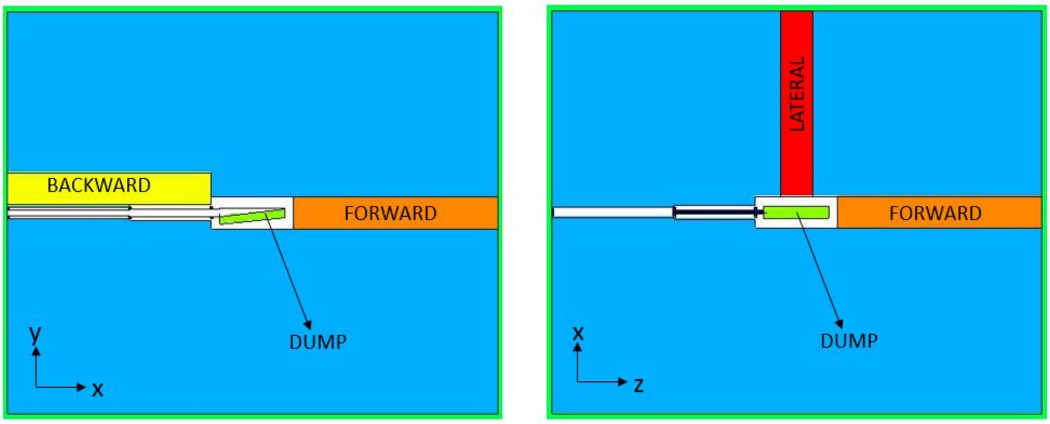

Figure 5.22: Volumes of concrete for which activation calculations are performed.

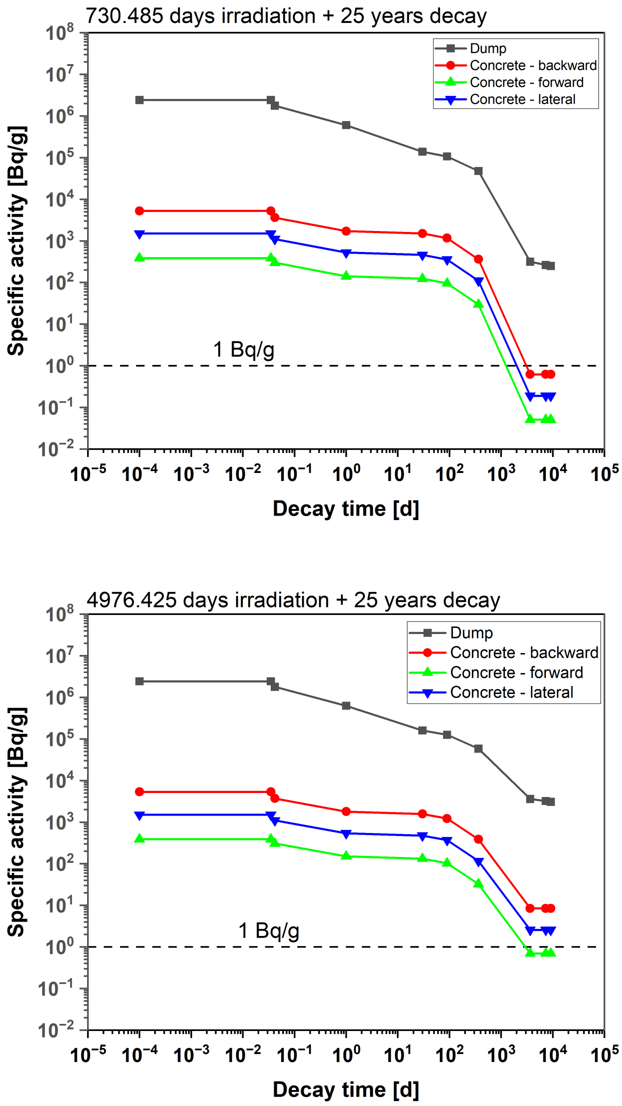

Figure 5.23: Specific activation for the beam dump and the concrete shield in two irradiation configurations

As it could be expected, the activation of the beam dump, on which the beam directly hits, is the highest. The specific activation of concrete is orders of magnitude smaller. The backward volume of concrete is the one that experiences the highest activation. This can be due to the presence of the void tube right close to it. In fact, secondary particles created by the interaction of the protons with the beam dump core have a preferential path in void rather than in concrete.
If the two irradiation histories are compared, it can be observed that specific activation is slightly greater for 4976.425 days of irradiation. Anyway, this difference is rather small until 1 year of decay. After that, a steeper decrease of the specific activity can be observed for the 730.485 days irradiation case. Due to this, the limit of clearance is reached for all the concrete layers after about 10 years. In the other case, only the frontal volume of concrete reaches the limit in the 25 years that have been studied. This difference may be due to the behavior of the single isotopic activities.
The main isotopic contributions to the activity of the beam dump and concrete (forward direction) are reported in Figure 5.24.
For the first year of decay, Zn-65 ($t_{1/2} = 244d$) is the main contributor to the activity of the beam dump core. After that, the main isotopic activity is the one of Ni-63($t_{1/2} = 91.6y$). The cumulative specific activity profile follows the same as of Zn-65 for the first year and, while this decays away, it settles to the Ni-63 value, which remained approximately constant since the beginning. Since after 4976.425 irradiation days the specific activity of Ni-63 is greater than the one after 730.485 days, the decrease of the cumulative specific activity will stop at a greater value for this case.
Similar observations can be done for concrete, in which Ca-45($t_{1/2} = 165d$) leaves its place to Ca-41($t_{1/2} = 9.94x10^4y$), after 1 year.
For completeness, the main isotopic contributions to the activities of the beam dump and of concrete are reported in Appendix C.

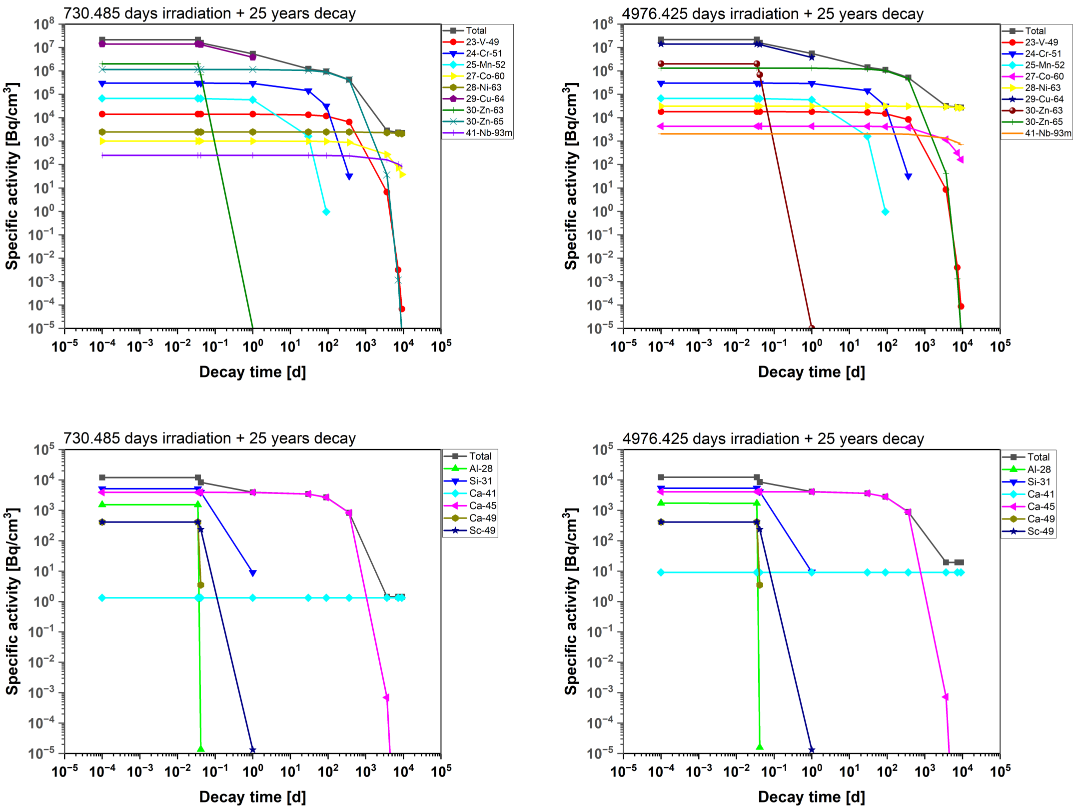

Figure 5.24: Contribution of the main isotopes to the activity of the beam dump core (top), and frontal volume of concrete (bottom).

Chapter 6

Conclusions and future perspectives

In the framework of the MYRRHA project, shielding and activation calculations for the injector have been performed.
The work has been organized in different tasks, related to the injector tunnel and to the injector beam dump. The main objective was to verify that dose rate limits imposed by the Belgian legislation and by SCK CEN are verified, thanks to shielding designs proposed by the institution or with solutions proposed by the author of the thesis. The approval of the project by the regulatory body is indeed based on the demonstration that the amount of radiation is limited in specific areas of the facility. In the injector tunnel, most of the radiation is due to the interaction of protons with the beam tube, which produces secondary radiation such as photons and neutrons. Moreover, the cumulative dose in the lighting fixtures inside the tunnel have been assessed in order to propose a maintenance and replacement strategy, and the activation of the beam dump and of its concrete shield have been computed. The activation of materials is particularly important for maintenance and for the waste management, after the final shut down of the facility.
The analysis was carried out by means of the Monte Carlo transport code MCNP6.2 and the depletion code ALEPH2. Thus, at first, these tools have been described and their working principles analysed, with a particular attention to the definition of relative error, the fundamental parameter used to assess the quality of the results. Variance reduction techniques, such as weight windows and DXTRAN spheres, have been studied and implemented, in order to speed up calculations and to obtain better statistics.
The level of complexity of the problem has been reduced by using a simplified, but conservative, geometry of the injector, in which not all of the components have been modelled. This provision permitted not only to have a better time management

(converting a complex 3D geometry in a MCNP geometry may be very challenging and time consuming), but most importantly, to improve the efficiency of the code. In fact, using more cells than those who are strictly needed could counter-balance the effect of variance reduction, in a very complex geometry.
The first task, the assessment of dose attenuation in the tunnel concrete shield, demonstrated that a 1 m thick concrete shield is enough to respect the dose limits, if the most realistic case (i.e. considering that protons are lost at different energies in different sections of the beam line) is modelled. A conservative approach, in which all protons are lost at the maximum energy, shows that the the dose rate in the furthest point of the shield from the particle source is slightly above the limit. Anyway, this may not lead to a change in the design because the approach was over-conservative.
The second task consisted in the estimation of the cumulative dose absorbed by the materials of the lighting fixtures inside the tunnel. It is well known that, when placed in a radiation field for a long period of time, some materials may experience radiation hardening. In conventional lighting fixtures, this phenomenon can be observed when 10 Gy are overcome. When this is the case, it is important to estimate a range for the absorbed dose, so that the right type of fixture will be requested by the operator to the producer. This study showed that the limit of 10y will be reached after about 10 years and an upper limit after 40 years of irradiation (the operational life of the injector) has been identified.
The last task related to the injector tunnel focused on the injector entrance, which is there to permit the access to the tunnel during commissioning and in case of maintenance. In compliance with the safety requirements of SCK CEN, a shielded door was designed. The proposed solution is a three-layers door: a central 15 cm layer of borated polyethylene (10 % Boron), and a 1 cm lead layer on both sides. Borated polyethylene showed to be good at stopping neutrons, while lead was very effective at shielding photons. It has been demonstrated that the dose rate at the entrance can be reduced by 60 times the original value, if this configuration is adopted.
The last part of the work focused on the beam dump. At first, the shielding effectiveness of a designed proposed at SCK CEN has been verified. For this purpose, two cases have been studied: reduced and full duty cycle. The simulations show that 2.50 m of standard concrete in forward and backward direction and 2.30 m in lateral direction are enough to shield prompt radiation in the reduced duty cycle. As far as the full duty cycle is concerned, the lateral thickness of the shield is not enough to comply with the limits. Thus an increase of thickness of concrete or the addition of other shielding materials is suggested.
Finally, the activation of the beam dump CuCrZr core and of the surrounding concrete has been calculated. As it could be expected, the beam dump core experiences much higher activation then concrete, because the proton beam directly

hits it. Moreover, it has been observed that concrete gets more activated in the backward direction, due to the design of the beam dump shield, which is characterised by the presence of a void tube to accommodate the beam tube that directs the beam towards the dump.
The work presented in this thesis give an outlook on the shielding design of the injector, but much more work needs to be done at SCK CEN. In particular, the same calculations may be repeated implementing the complete geometry, modelling all the components and assessing what are the main differences with the conservative case, presented in this work. As a continuation of the injector entrance task, other shielded door designs may be tested (changing materials, layers configuration etc.), with objective of reducing the total thickness of the door. As far as the beam dump is concerned, the shielding can be improved also for the full duty cycle case, by adding different shielding materials or increasing the concrete thickness.
In conclusion, these findings are a first step in the shielding design of the MYRRHA injector beam line, and may serve as a base for future deeper and more detailed analysis.

Appendix A

Material composition

In this section, the compositions of some of the main materials used in the simulations are presented. Standard concrete is used as a shielding material. SS316L is the material of the beam tube. Borated polyethylene and SS304 are used in the design of the shielded door.

Table A.1: Elemental composition of standard concrete. Density is 2.3 g/cm3

Element	**Weight in %**
O	53
Si	37.2
Ca	8.3
H	1.0
Mg	0.5

Table A.2: Elemental composition of SS316L. Density is 8.00 g/cm3

Element	**Weight in %**
C	0.03
Mn	2
P	0.045
S	0.03
Si	1
Cr	17
Ni	12
Mo	2.5
Fe	65.395

Table A.3: Elemental composition of borated polyethylene. Density is 1 g/cm3

Element	**Weight in %**
H	12.53
B	10.00
C	77.47

Table A.4: Elemental composition of SS304. Density is 8.03 g/cm3

Element	**Weight in %**
C	0.080
Mn	2.000
P	0.045
S	0.030
Si	1.000
Cr	19.000
Ni	9.500
Fe	68.345

Table A.5: Elemental composition of CuCrZr. Density is 8.94 g/cm3

Element	**Weight in %**
Cu	99.15
Cr	0.7
Zr	0.15

Appendix B

Protons energy

Table B.1: Protons' energies at the end of different component [30]

Component	Start position [m]	Active length [m]	Energy [MeV]
Source	0	0	0.03
RFQ	2.7	4.02	1.52
QWR1	6.8665	0.2	1.52
QWR2	7.6605	0.2	1.52
CH1	8.1615	0.312	1.719
CH2	8.7256	0.375	2.022
CH3	9.3525	0.451	2.464
CH4	10.057	0.545	3.057
CH5	10.855	0.659	3.81
CH6	11.768	0.879	4.859
CH7	12.9	0.957	5.879
CHR	14.645	0.616	5.879
CH8	15.874	1.24	7.26
CH9	17.552	1.5	8.73
CH10	19.462	1.61	10.18
CH11	21.478	1.58	11.53
CH12	23.46	1.52	12.83
CH13	25.381	1.58	14.129
CH14	27.365	1.5	15.379
CH15	29.255	1.55	16.639
SpokeR1	34.203	0.415	16.639
SpokeR2	41.505	0.415	16.639
SpokeR3	44.174	0.415	16.639

Appendix C

Beam dump activation

In the following tables, the main contributions to the activation of the CuCrZr beam dump core, and of the three layers of concrete that have been considered are collected. These are the results obtained for an irradiation period of 730.485 days.

Table C.1: Main isotopic contributions to the activity in of concrete, backward direction. Results in in Bq/cm^3.

Decay time	**C-14**	**Al-28**	**Si-31**	**Ca-41**
1 s	8.97E-02	1.53E+03	5.15E+03	1.32E+00
1 h	8.97E-02	1.36E-05	3.95E+03	1.32E+00
1 d	8.97E-02	0.00E+00	8.99E+00	1.32E+00
1 m	8.97E-02	0.00E+00	0.00E+00	1.32E+00
3 m	8.97E-02	0.00E+00	0.00E+00	1.32E+00
1 y	8.97E-02	0.00E+00	0.00E+00	1.32E+00
10 y	8.96E-02	0.00E+00	0.00E+00	1.32E+00
20 y	8.95E-02	0.00E+00	0.00E+00	1.32E+00
25 y	8.95E-02	0.00E+00	0.00E+00	1.32E+00
Decay time	**Ca-45**	**Ca-48**	**Ca-49**	**Sc-49**
1 s	3.90E+03	1.86E-09	4.11E+02	4.11E+02
1 h	3.90E+03	1.86E-09	3.49E+00	2.34E+02
1 d	3.89E+03	1.86E-09	0.00E+00	1.31E-05
1 m	3.44E+03	1.86E-09	0.00E+00	0.00E+00
3 m	2.66E+03	1.86E-09	0.00E+00	0.00E+00
1 y	8.24E+02	1.86E-09	0.00E+00	0.00E+00
10 y	6.91E-04	1.86E-09	0.00E+00	0.00E+00
20 y	1.26E-10	1.86E-09	0.00E+00	0.00E+00
25 y	4.92E-13	1.86E-09	0.00E+00	0.00E+00

Table C.2: Main isotopic contributions to the activity of concrete, forward direction. Results in in Bq/cm^3.

Decay time	**C-14**	**Si-31**	**Ca-41**	**Ca-45**
1 s	6.68E-03	4.11E+02	1.05E-01	3.10E+02
1 h	6.68E-03	3.16E+02	1.05E-01	3.10E+02
1 d	6.68E-03	7.19E-01	1.05E-01	3.09E+02
1 m	6.67E-03	0.00E+00	1.05E-01	2.73E+02
3 m	6.67E-03	0.00E+00	1.05E-01	2.11E+02
1 y	6.67E-03	0.00E+00	1.05E-01	6.54E+01
10 y	6.67E-03	0.00E+00	1.05E-01	5.45E-05
20 y	6.66E-03	0.00E+00	1.05E-01	1.06E-11
25 y	6.65E-03	0.00E+00	1.05E-01	0.00E+00
Decay time	**Ca-48**	**Ca-49**	**Sc-49**	
1 s	1.86E-09	3.27E+01	3.27E+01	
1 h	1.86E-09	2.78E-01	1.86E+01	
1 d	1.86E-09	0.00E+00	1.07E-06	
1 m	1.86E-09	0.00E+00	0.00E+00	
3 m	1.86E-09	0.00E+00	0.00E+00	
1 y	1.86E-09	0.00E+00	0.00E+00	
10 y	1.86E-09	0.00E+00	0.00E+00	

Table C.3: Main isotopic contributions to the activity of concrete, lateral direction. Results in in Bq/cm^3.

Decay time	**C-14**	**Al-28**	**Si-31**	**Ca-41**
1 s	2.68E-02	2.87E+02	1.59E+03	4.14E-01
1 h	2.68E-02	2.78E-06	1.22E+03	4.14E-01
1 d	2.68E-02	0.00E+00	2.78E+00	4.14E-01
1 m	2.68E-02	0.00E+00	0.00E+00	4.14E-01
3 m	2.68E-02	0.00E+00	0.00E+00	4.14E-01
1 y	2.68E-02	0.00E+00	0.00E+00	4.14E-01
10 y	2.68E-02	0.00E+00	0.00E+00	4.14E-01
20 y	2.68E-02	0.00E+00	0.00E+00	4.14E-01
25 y	2.68E-02	0.00E+00	0.00E+00	4.14E-01
Decay time	**Ca-45**	**Ca-48**	**Ca-49**	**Sc-49**
1 s	1.22E+03	1.86E-09	1.28E+02	1.29E+02
1 h	1.22E+03	1.86E-09	1.09E+00	7.31E+01
1 d	1.21E+03	1.86E-09	0.00E+00	4.03E-06
1 m	1.07E+03	1.86E-09	0.00E+00	0.00E+00
3 m	8.31E+02	1.86E-09	0.00E+00	0.00E+00
1 y	2.57E+02	1.86E-09	0.00E+00	0.00E+00
10 y	2.16E-04	1.86E-09	0.00E+00	0.00E+00

Table C.4: Main isotopic contributions to the activity of the beam dump core. Results in in Bq/cm^3.

Decay time	**V-49**	**Cr-50**	**Cr-51**	**Mn-52**	**Co-60**	**Ni-63**	**Cu-62**
1 s	1.42E+04	3.71E-05	2.97E+05	6.67E+04	9.28E+02	2.42E+03	5.67E+05
1 h	1.42E+04	3.71E-05	2.96E+05	6.64E+04	9.28E+02	2.42E+03	5.50E+04
1 d	1.41E+04	3.71E-05	2.89E+05	5.89E+04	9.28E+02	2.42E+03	8.44E+03
1 m	1.33E+04	3.71E-05	1.40E+05	1.62E+03	9.18E+02	2.42E+03	0.00E+00
3 m	1.17E+04	3.71E-05	3.12E+04	9.59E-01	8.99E+02	2.42E+03	0.00E+00
1 y	6.57E+03	3.71E-05	3.21E+01	0.00E+00	8.14E+02	2.40E+03	0.00E+00
10 y	6.63E+00	3.71E-05	0.00E+00	0.00E+00	2.49E+02	2.26E+03	0.00E+00
20 y	3.10E-03	3.71E-05	0.00E+00	0.00E+00	6.70E+01	2.10E+03	0.00E+00
25 y	6.72E-05	3.71E-05	0.00E+00	0.00E+00	3.47E+01	2.03E+03	0.00E+00
Decay time	**Cu-64**	**Cu-66**	**Zn-63**	**Zn-65**	**Zr-94**	**Nb-91**	**Nb-93m**
1 s	1.39E+07	2.93E+06	2.02E+06	1.16E+06	2.78E-05	2.57E+01	2.46E+02
1 h	1.31E+07	8.45E+02	6.82E+05	1.16E+06	2.78E-05	2.57E+01	2.46E+02
1 d	3.74E+06	0.00E+00	1.02E-05	1.15E+06	2.78E-05	2.57E+01	2.46E+02
1 m	0.00E+00	0.00E+00	0.00E+00	1.06E+06	2.78E-05	2.60E+01	2.45E+02
3 m	0.00E+00	0.00E+00	0.00E+00	8.95E+05	2.78E-05	2.64E+01	2.43E+02
1 y	0.00E+00	0.00E+00	0.00E+00	4.10E+05	2.78E-05	2.68E+01	2.36E+02
10 y	0.00E+00	0.00E+00	0.00E+00	3.63E+01	2.78E-05	2.66E+01	1.60E+02
20 y	0.00E+00	0.00E+00	0.00E+00	1.14E-03	2.78E-05	2.63E+01	1.04E+02
25 y	0.00E+00	0.00E+00	0.00E+00	6.42E-06	2.78E-05	2.62E+01	8.40E+01

Bibliography

[1] H. Aït Abderrahim et al. «Accelerator driven subcritical systems». In: *E. Greenspan (Ed.), Encyclopedia of Nuclear Energy, Elsevier, Oxford, pp. 191–202* (2021) (cit. on pp. 1, 2, 5).

[2] *SCK CEN (Belgian nuclear research center).* `https://www.sckcen.be/en/infrastructure/myrrha/myrrha-phase-1-minerva` (cit. on p. 1).

[3] Christopher John Werner et al. «MCNP User's Manual Code Version 6.2.» In: *Los Alamos National Laboratory LA-UR-17-29981, Los Alamos, NM, USA* (2017) (cit. on pp. 3, 9, 10, 12–16).

[4] A. Stankovskiy and G. Van den Eynde. «Advanced Method for Calculations of Core Burn-Up, Activation of Structural Materials, and Spallation Products Accumulation in Accelerator-Driven Systems». In: *Science and Technology of Nuclear Installations, vol. 2012, 545103* (2012) (cit. on pp. 3, 9).

[5] S. Voorderhake. «Requirements – Sub-Programme Documentation». In: *SCK CEN/35576097* (2020) (cit. on p. 5).

[6] R. Salemme et al. «Design progress of the MYRRHA low energy beam line». In: *Proceedings of LINAC2014, Geneva, Switzerland, paper MOPP137* (2014) (cit. on p. 6).

[7] H. Podlech et al. «The MYRRHA RFQ - Status and first measurements». In: *Proceedings of IPAC2017, Copenhagen, Denmark, paper TUPVA071* (2017) (cit. on p. 6).

[8] P. Müller et al. «RF SIMULATIONS OF THE INJECTOR SECTION FROM CH8 TO CH15 FOR MYRRHA». In: *Proc. 9th International Particle Accelerator Conference (IPAC'18), Vancouver, BC, Canada, pp. 2790-2792, paper WEPML043* (2018) (cit. on p. 6).

[9] *Bijlage III. Koninklijk besluit van 20 juli 2001 houdende algemeen reglement op de bescherming van de bevolking, van de werknemers en het leefmilieu tegen het gevaar van de ioniserende stralingen.* `https://www.jurion.fanc.fgov.be/jurdb-consult/consultatieLink?wettekstId=11564&appLang=nl&wettekstLang=nl` (cit. on p. 8).

[10] «The 2007 Recommendations of the International Commission on Radiological Protection». In: *Annals of ICPR, ICRP Publication 103* (2007) (cit. on p. 8).

[11] D. Ene. «Radioprotection Studies for the ESS Superconducting Linear Accelerator Preliminary Estimates». In: *ESS AD Technical Note/003* (2010) (cit. on p. 8).

[12] A.J.Koning et al. «TENDL: Complete Nuclear Data Library for Innovative Nuclear Science and Technology». In: *Nuclear Data Sheets 155* (2019) (cit. on p. 9).

[13] A. J. Koning et. al. «TENDL: Complete Nuclear Data Library for Innovative Nuclear Science and Technology». In: *Nuclear Data Sheets 155* (2019) (cit. on p. 9).

[14] Ionel Michael Navon D.G. Cacuci Mihaela Ionescu-Bujor. «Sensitivity and uncertainty analysis.» In: *Chapman Hall/CRC Press, 2003. ISBN: 1584881151* () (cit. on p. 11).

[15] Thomas E. Booth. «A SAMPLE PROBLEM FOR VARIANCE REDUCTION IN MCNP». In: *Los Alamos National Laboraty, LA-10363-MS* (1985) (cit. on p. 11).

[16] John S. Hendricks Christopher N. Culbertson. «An Assessment of the MCNP4C Weight Window». In: *Los Alamos National Laboraty, LA-13668* (1999) (cit. on p. 14).

[17] K. C. Kelley T. E. Booth and S. S. McCready. «Monte Carlo Variance Reduction Using Nested Dxtran Spheres». In: *Nuclear Technology* 168.3 (2009), pp. 765–767. DOI: 10.13182/NT09-A9303 (cit. on p. 15).

[18] D. Ene et al. «Radiation Protection Studies for ESS Superconducting Linear Accelerator». In: *Progress in NUCLEAR SCIENCE and TECHNOLOGY, Vol. 2, pp.382-388* (2011) (cit. on p. 20).

[19] S. Agosteo and M. Silari. «Preliminary shielding calculations for a 2 GeV superconducting proton LINAC». In: *CERN NUFACT Note 088* (2001) (cit. on p. 20).

[20] Y. O. Lee et al. «Preliminary Shielding Assessment for the 100 MeV Proton LINAC (KOMAC)». In: *Radiation Protection dosimetry, vol. 115, 569-572* (2005) (cit. on p. 20).

[21] R. Daneels. «Estimation of the maximum beam stop time interval». In: *Technical report, SCK CEN/43659984* (2021) (cit. on p. 20).

[22] M. Pelliccioni. «Overview of Fluence-to-Effective Dose and Fluence-to-Ambient Dose Equivalent Conversion Coefficients for High Energy Radiation Calculated using the Fluka Code». In: *Radiation Protection Dosimetry 88 (2000) 279–297* () (cit. on p. 23).

[23] H. O. Tekin et al. «Photon and neutron shielding performance of boron phosphate glasses for diagnostic radiology facilities». In: *Results in Physics 12, 1457-1464* (2019) (cit. on p. 40).

[24] Y. Huang et al. «A “Sandwich” type of neutron shielding composite filled with boron carbide reinforced by carbon fiber». In: *Chem. Eng. J., 220* (2013) (cit. on p. 40).

[25] A. El-Sayed Abdo A.M. El-Khayatt. «MERCSF-N: A program for the calculation of fast neutron removal cross sections in composite shields». In: *Annals of Nuclear Energy 36(6) (2009) 832-836* () (cit. on p. 40).

[26] E. A. Amirabadi et al. «Study of Neutron and Gamma Radiation Protective Shield». In: *International Journal of Innovation and Applied Studies, 3(4) (2013) pp. 1079-1085* () (cit. on p. 40).

[27] W. Chen J. Lu. «High effective shielding material lead-baron polyethylene». In: *Nuclear Power Engineering, 15(4) (1994) 370-374* () (cit. on p. 40).

[28] Zeinab Y. Alsmad. «Shielding Properties of Alloy 709 Advanced Austenitic Stainless Steel as Candidate Canister Material in Spent Fuel Dry Casks». In: *International Journal of Physics and Research, DOI: 10.24247/ijprdec20202* (2020) (cit. on p. 42).

[29] J.M. Fernández-Varea F. Salvat. «Overview of physical interaction models for photon and electron transport used in Monte Carlo codes». In: *Metrologia* (2009) (cit. on p. 42).

[30] A. Gatera. «Energy gain and position per cavity (MeV)». In: *Technical report, SCK CEN/43215551* (2019) (cit. on p. 61).